Linking Lithospheric Structure, Mantle Flow and Intra-Plate Volcanism

Thomas Duvernay[1], **D. Rhodri Davies**[1], **Christopher R. Mathews**[1], **Angus H. Gibson**[1], **Stephan C. Kramer**[2]

[1]Research School of Earth Sciences, Australian National University, Canberra, ACT, Australia
[2]Department of Earth Science and Engineering, Imperial College London, London, UK

Key Points:

- Spatial and temporal characteristics of edge-driven convection are sensitive to the geometry and material properties of lithospheric steps.
- Asthenospheric flow magnitude and orientation dictate whether edge-driven cells are enhanced through shear-driven upwelling, or suppressed.
- Melting associated with these processes can account for Earth's shorter-lived and lower-volume intra-plate volcanic provinces.

Corresponding author: Thomas Duvernay, thomas.duvernay@anu.edu.au

Abstract

Several of Earth's intra-plate volcanic provinces are difficult to reconcile with the mantle plume hypothesis. Instead, they exhibit characteristics that are better explained by shallower processes involving the interplay between uppermost mantle flow and the base of Earth's heterogeneous lithosphere. The mechanisms most commonly invoked are edge-driven convection (EDC) and shear-driven upwelling (SDU), both of which act to focus upwelling flow, and the associated decompression melting, adjacent to steps in lithospheric thickness. In this study, we undertake a systematic numerical investigation, in both 2-D and 3-D, to quantify the sensitivity of EDC, SDU and their associated melting to several key controlling parameters. Our simulations demonstrate that the spatial and temporal characteristics of EDC are sensitive to the geometry and material properties of the lithospheric step, in addition to the depth-dependence of upper mantle viscosity. These simulations also indicate that asthenospheric shear can either enhance or reduce upwelling velocities and predicted melt volumes, depending upon the magnitude and orientation of flow relative to the lithospheric step. When combined, such sensitivities explain why step changes in lithospheric thickness, which are common along cratonic edges and passive margins, only produce volcanism at isolated points in space and time. Our predicted trends of melt production suggest that, in the absence of potential interactions with mantle plumes, EDC and SDU are viable mechanisms only for Earth's shorter-lived, lower-volume intra-plate volcanic provinces.

Plain Language Summary

Intra-plate volcanoes, which occur away from plate boundaries, are common across Earth's surface (e.g. Hawaii, Reunion, Cameroon and Eastern Australia), but their origin remains debated. Diverse driving mechanisms have been proposed, most notably mantle plumes – buoyant columns of hot rocks that ascend vigorously through Earth's mantle. Upon reaching the base of tectonic plates, plumes generate extensive melting and remain approximately fixed. As a result, they explain particularly well the origin of linear volcanic tracks that grow older in the direction of plate motion. Several intra-plate volcanic regions, however, exhibit characteristics that are inconsistent with the mantle plume hypothesis. They are often short-lived, of low volume and do not display a clear age-progression. As such, they are better explained by shallower processes, driven by small-scale convective instabilities that develop adjacent to step-changes in lithospheric thickness. In this study, we utilise both 2-D and 3-D computational models to simulate these shallow processes and to analyse their sensitivity to a range of geological settings and material properties. Our results help to solve the puzzle of why these processes only produce volcanism at isolated locations, and, in the absence of interactions with mantle plumes, limit their applicability to Earth's shorter-lived, lower-volume volcanic provinces.

1 Introduction

Most of Earth's volcanism is concentrated at tectonic plate boundaries, representing the surface manifestation of either passive decompression melting at mid-ocean ridges (e.g. Sengör & Burke, 1978; Phipps Morgan et al., 1987) or volatile-induced melting at subduction zones (e.g. Tatsumi et al., 1986; Peacock, 1990). However, a significant and widespread class of volcanism occurs within plates or across plate boundaries. These so-called *intra-plate* volcanic provinces (Turcotte & Oxburgh, 1978) cannot be explained through plate tectonic processes and require an alternative generation mechanism. Mantle plumes – hot, buoyant columns that rise from Earth's core-mantle boundary to its surface (Morgan, 1971, 1972) – are commonly invoked to explain age-progressive volcanic provinces that grow older in the direction of plate motion. At these locations, volcanism has persisted for tens of millions of years and is localised within a radius of a few tens of kilometres, implying a self-renewing source that lies below the region where the

mantle moves with the surface plate (e.g. Richards & Griffiths, 1989; Richards et al., 1989; Farnetani & Richards, 1995; Courtillot et al., 2003; Davies & Davies, 2009; French & Romanowicz, 2015). Classic examples include the volcanic tracks terminating at Hawaii in the Pacific, Reunion in the Indian Ocean and Cosgrove in eastern Australia (e.g. Ballmer et al., 2011; Davies et al., 2015; Jones et al., 2017; Bredow et al., 2017). However, many intra-plate volcanic provinces are difficult to reconcile with the mantle plume hypothesis, such as the Colorado Plateau in North America, the Moroccan Atlas Mountains in northern Africa and the Newer Volcanics Province of south-eastern Australia (e.g. Thompson & Zoback, 1979; Demidjuk et al., 2007; Missenard & Cadoux, 2012; Boyce, 2013; Davies & Rawlinson, 2014). At these locations, volcanism is often short-lived (< 20 Myr), generally of low eruptive volume, and does not show a clear age-progression in the direction of plate motion, requiring an alternative generation mechanism (e.g. Davies & Rawlinson, 2014; Ballmer et al., 2015).

Several mechanisms have been proposed, with the majority involving the interplay between shallow mantle flow and the base of Earth's heterogeneous lithosphere. The two most commonly invoked are (i) edge-driven convection (EDC) – a small-scale convective instability, associated with a step in lithospheric thickness, driven by lateral density variations between a thick lithosphere and adjacent asthenosphere (e.g. Buck, 1986; King & Anderson, 1998; Farrington et al., 2010; Till et al., 2010; Davies & Rawlinson, 2014; Ballmer et al., 2015; Liu & Chen, 2019) – and (ii) shear-driven upwelling (SDU) – sub-lithospheric ascending flow, induced by topography at the base of the lithosphere in the presence of asthenospheric shear (e.g. Conrad et al., 2010, 2011; Bianco et al., 2011; Ballmer et al., 2013; Davies & Rawlinson, 2014; Ballmer et al., 2015). Low-viscosity pockets in the shallow asthenosphere have also been shown to facilitate SDU (e.g. Conrad et al., 2010), but we focus on the role of lithospheric topography here. The applicability and relative importance of EDC and SDU remains unclear and likely varies from one volcanic province to the next, as a consequence of regional differences in the primary controlling parameters (e.g. Conrad et al., 2010, 2011; Davies & Rawlinson, 2014; Ballmer et al., 2015). To complicate matters further, EDC and SDU may interact with upwelling mantle plumes and pockets of low-viscosity asthenosphere to produce intricate volcanic patterns at the surface (e.g. Conrad et al., 2011; Davies et al., 2015; Ballmer et al., 2015; Rawlinson et al., 2017; Kennett & Davies, 2020).

To better understand these interactions and isolate the role of each process, it is necessary to analyse, in isolation, how EDC, SDU and the associated melting depend on several possible controlling parameters. Accordingly, in this study, we use a systematic series of 2-D and 3-D numerical models to quantify the sensitivity of EDC and SDU to a subset of these parameters: (i) the topography of the lithosphere-asthenosphere boundary (LAB), especially the geometry and orientation of lithospheric steps and their material properties; (ii) uppermost mantle viscosity, both in terms of its magnitude and depth-dependence; and (iii) the intensity, depth distribution and orientation of background mantle flow. These models allow us to identify the fundamental controls on shallow edge-related processes and highlight, in particular, what determines the location and intensity of melt production at depth. Our results allow us to place bounds on the conditions under which EDC and SDU can explain intra-plate volcanism in the absence of other melt-generating processes.

2 Methods

2.1 Governing Equations and Solution Strategy

We set up a numerical study of thermo-chemical convection applied to Earth's mantle in both 2-D and 3-D Cartesian domains with dimensions 5000:[4000]:1000 km (x:[y]:z). We use Fluidity – a finite-element, control-volume computational modelling framework (e.g. Davies et al., 2011; Kramer et al., 2012) – to solve the equations governing man-

tle convection for pressure, velocity and temperature fields on an anisotropic, adaptive, simplex mesh. Mesh optimisation is controlled by a metric that depends on curvatures of the temperature, velocity, material volume fraction (Section 2.2 or, for further information, Davies et al., 2011) and melt fraction fields (Section 2.4). It provides increased resolution in areas of dynamical significance, with coarser resolution elsewhere, thus ensuring computational efficiency whilst maintaining solution accuracy. The resulting mesh satisfies a minimum edge-length condition of 5 km, a maximum edge-length of 200 km and a 30 % edge-length gradation (i.e. the maximum allowable jump in edge-length from element to element).

We simulate incompressible (Boussinesq) Stokes flow in an Eulerian reference frame, incorporating spatial variations of viscosity. In this context, we solve the following governing equations:

$$0 = \nabla \cdot \boldsymbol{u}, \tag{1}$$

$$\boldsymbol{0} = \nabla p - \nabla \cdot \left[\mu\Big(\nabla \boldsymbol{u} + (\nabla \boldsymbol{u})^{\mathsf{T}}\Big)\right] + \rho_0 \alpha \big(T - T_S\big)\boldsymbol{g}, \tag{2}$$

$$\mu = \left(A_1 \times \exp\Big(-\frac{E^* + \rho_0 g z\, V_1^*}{RT^*}\Big) + A_2 \times \exp\Big(-\frac{E^* + \rho_0 g z\, V_2^*}{RT^*}\Big)\right)^{-1}, \tag{3}$$

$$\rho = \rho_0\Big(1 - \alpha\big(T - T_S\big)\Big), \tag{4}$$

$$T^* = T + \psi z. \tag{5}$$

We model energy conservation through a simple advection-diffusion equation including a heat source term,

$$\frac{\partial T}{\partial t} + \boldsymbol{u} \cdot \nabla T = \kappa \Delta T + \phi. \tag{6}$$

In the above equations, $\boldsymbol{u}$ denotes the velocity, p the dynamic pressure, μ the dynamic viscosity, T the (potential) temperature, z the depth and ρ the density. Other symbol names and values are presented in Tables 1 and 2.

2.2 2-D Reference Case

We begin by simulating idealised 2-D flow around a thermally and compositionally-defined step in lithospheric thickness which separates thick continental lithosphere from thin oceanic lithosphere, analogous to a passive margin setting. We make use of Fluidity's multi-material functionality (Wilson, 2009) which allows, for example, independent equations of state and rheological laws to be applied to individual materials in separate parts of the domain (e.g. Garel et al., 2014). In our models, we include three different materials, namely: continental crust, continental lithosphere (excluding the crust) and mantle (incorporating oceanic lithosphere). Each has a distinct density (Table 1; Kaban et al., 2003; Artemieva, 2009), but they all obey the same viscosity law, albeit with continental lithosphere that is intrinsically 100 times more viscous than adjacent mantle (e.g. Lenardic & Moresi, 1999; Lenardic et al., 2003; Wang et al., 2014; Currie & van Wijk, 2016).

We consider viscosity, μ, to be isotropic and model it through a diffusion creep rheology. To describe this mechanical behaviour, we combine two empirical Arrhenius laws (Hirth & Kohlstedt, 2004; Korenaga & Karato, 2008) inside which we account for both the temperature increase through the adiabatic gradient, ψ, and the effect of lithostatic pressure (Equations 3 and 5). We fix a common activation energy, E^*, for both laws but vary the activation volumes, V_i^*, and viscosity pre-factors, A_i. By setting distinct V_1^* and V_2^* in Equation 3, we can incorporate a low-viscosity channel in the sub-lithospheric mantle (e.g. Richards et al., 2001). Conversely, specifying identical parameters across both equations leads to a single law with a pre-factor twice as large. To determine V_i^* and A_i and, thereby, establish our upper mantle viscosity profile, we consider a thermal

Table 1. *Model Parameters Common to All Simulations*

Name	Symbol	Value	Units
Reference Density	$\rho_0 \,\vert\, \rho_0^{Cont} \,\vert\, \rho_0^{Crust}$	$3370 \,\vert\, 3300 \,\vert\, 2900$[a]	$\mathrm{kg\,m^{-3}}$
Gravity	g	9.8	$\mathrm{m\,s^{-2}}$
Gas Constant	R	8.3145	$\mathrm{J\,K^{-1}\,mol^{-1}}$
Thermal Expansion	α	3×10^{-5}[b]	$\mathrm{K^{-1}}$
Surface Temperature	T_S	290	K
Mantle Potential Temperature	T_P	1650[c,d]	K
Adiabatic Gradient	ψ	4×10^{-4}[e]	$\mathrm{K\,m^{-1}}$
Thermal Diffusion	κ	6×10^{-7}[f,g]	$\mathrm{m^2\,s^{-1}}$
Internal Heating (Cont. Crust)	ϕ	2.6×10^{-13}[h]	$\mathrm{K\,s^{-1}}$
Internal Heating (Elsewhere)	ϕ	4×10^{-15}[i]	$\mathrm{K\,s^{-1}}$
Activation Energy	E^*	350	$\mathrm{kJ\,mol^{-1}}$
Upper Mantle Viscosity at ULMB	μ_{660}	10^{21}	Pa s
Lower Mantle Viscosity	μ_{LM}	2×10^{22}	Pa s
Viscosity Bounds	$\mu_{min} \,\vert\, \mu_{max}$	$10^{18} \,\vert\, 10^{24}$	Pa s

Note. Parameters for the rheological law are guided by Korenaga and Karato (2008); values chosen for the upper mantle can be found in Table 2.
[a] Artemieva (2009). [b] Ye et al. (2009). [c] Putirka (2016). [d] Sarafian et al. (2017). [e] Katsura et al. (2010). [f] Gibert et al. (2003). [g] Whittington et al. (2009). [h] $\equiv 1.3 \times 10^{-6}\,\mathrm{W\,m^{-3}}$ (Jaupart & Mareschal, 2005). [i] $\equiv 2 \times 10^{-8}\,\mathrm{W\,m^{-3}}$ (Pollack & Chapman, 1977).

structure generated by a half-space cooling model (Parsons & Sclater, 1977) of age 40 Myr and define target values that the profile should satisfy. These are (i) μ_{660}, the value at the upper-lower mantle boundary (ULMB; Mitrovica & Forte, 2004; Lau et al., 2016; Métivier et al., 2016) which we set to 10^{21} Pa s; and (ii) μ^0_{min}, the profile's minimum attained value in the immediate sub-lithospheric mantle (Fjeldskaar & Cathles, 1991; Naif et al., 2013; Iaffaldano & Lambeck, 2014). Additionally, we specify if an asthenospheric low-viscosity channel is to be included (e.g. Rolf et al., 2018), in which case parameters differ across both laws. Using these constraints, we iteratively determine the values of pre-factors A_i and activation volumes V_i^* (Table 2). To complete our profile, we fix the lower-mantle viscosity, μ_{LM}, to 2×10^{22} Pa s, resulting in a factor of 20 increase through the ULMB. Finally, viscosity is bounded by $\mu_{min} = 10^{18}$ Pa s and $\mu_{max} = 10^{24}$ Pa s. The resulting profiles, which are used in this study, are illustrated in Figure 1a; they are compatible with estimates derived from models of global isostatic adjustment (e.g. Mitrovica & Forte, 2004; Paulson & Richards, 2009; Lau et al., 2016).

For our reference model, we impose no-slip velocity boundary conditions at the bottom of the domain and free-slip boundary conditions elsewhere. The temperature is set to $T_S = 290$ K at the surface and $T_P = 1650$ K at the base, with zero heat transfer on side boundaries: $\frac{\partial T}{\partial n} = 0$. Initial temperature conditions incorporate a sub-lithospheric mantle of temperature T_P and differentiate between oceanic and continental realms (Figure 1c). Oceanic lithosphere is treated as a surface thermal boundary layer, where the temperature distribution follows a half-space cooling model of age 40 Myr; the 1620 K isotherm, which we use to identify the LAB, is located at a depth of 90 km. Thicker continental lithosphere, including a 41 km-thick crust, extends down to 200 km depth and is described by a conductive geotherm (e.g. Pollack & Chapman, 1977; McKenzie et al., 2005) which we determine by solving a steady-state one-dimensional heat equation. We use a value of $3\,\mathrm{W\,m^{-1}\,K^{-1}}$ for the thermal conductivity (Schatz & Simmons, 1972) and account for internal heat generation through an exponential decrease of characteristic length-scale 9 km (e.g. Lachenbruch, 1970) and a surface crustal heat production of $6 \times 10^{-6}\,\mathrm{W\,m^{-3}}$ (Neumann et al., 2000; McLaren et al., 2003). The latter heat production is compati-

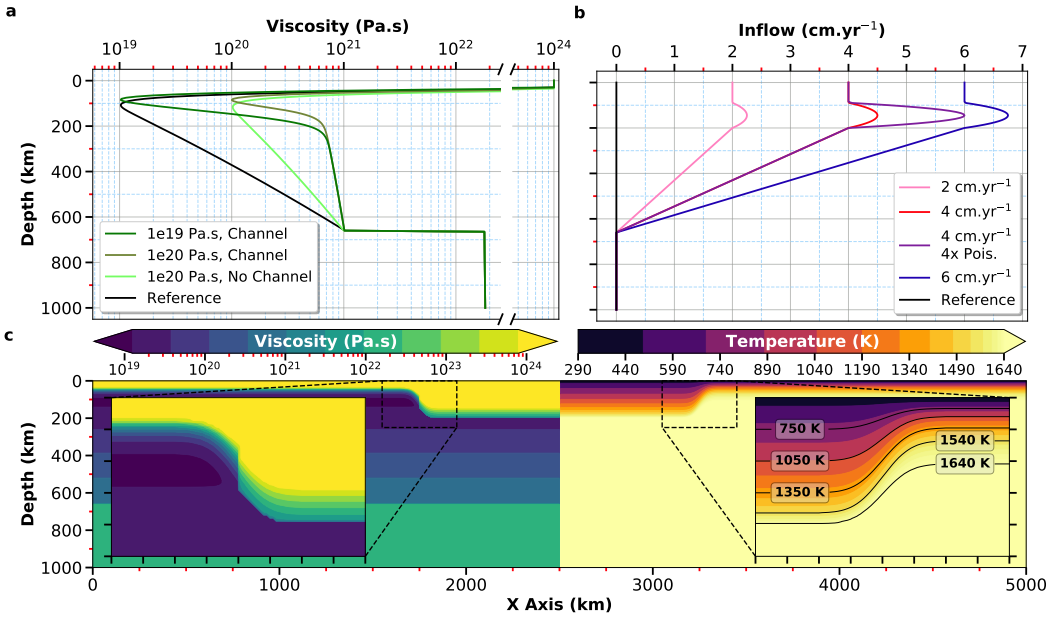

Figure 1. Model setup for 2-D simulations. (a) Viscosity profiles considered in the 2-D parameter space study, calculated according to the temperature distribution of the reference 40 Myr old oceanic lithosphere. (b) Velocity profiles used at the inflow boundary. The Poiseuille component is $\frac{1}{8}$ of the lithospheric speed, except for the case with additional shear where it is $\frac{1}{2}$. (c) Initial distribution of viscosity (left) and temperature (right) inside the 2-D domain. The viscosity inset illustrates the separation between continent and ocean through the $\times 100$ continental viscosity increase, while the temperature inset highlights the smooth paths taken by isotherms at the step.

ble with the internal heating, ϕ, defined in Equation 6, as it yields a comparable heat flux upon integration (Nicolaysen et al., 1981; Jaupart et al., 1998; Jaupart & Mareschal, 2005). Oceanic and continental segments are connected via two 200 km-wide thermal steps located between 1650 km and 1850 km to the left, and 3150 km and 3350 km to the right of the continent. Within these steps, the depth of a given isotherm follows an error function of the horizontal coordinate, x. Such a definition ensures a smooth, diffusive transition between the continental area and adjacent lithosphere (Figure 1c).

2.3 Parameter Space

2.3.1 2-D Cases

To assess possible expressions of flow adjacent to lithospheric steps, we first conduct a systematic study around our reference case, exploring a range of values for potential key, controlling parameters (Table 2). We vary four geometric parameters: the initial age of oceanic lithosphere (i.e. the thickness of the lithospheric lid), the depth of the continent, the width of the lithospheric step, and the location of the material interface between continent and ocean within the step. We also examine four distinct viscosity profiles (Figure 1a), which share their value of μ_{660} but differ by their μ^0_{min} and the presence, or absence, of a sub-lithospheric viscosity channel. Furthermore, we investigate the effect of background flow through kinematic boundary conditions: whilst keeping the surface free-slip, we apply four horizontal inflow profiles at the left boundary, where $x = 0$ km (Figure 1b), leaving the outflow boundary free, albeit with a prescribed litho-

Table 2. *Model Parameters Varied Across 2-D Simulations*

Geometry		
Name	Values	Units
Oceanic Lithosphere Age	20, **40** and 60	Myr
Continent Depth	140 and **200**	km
Step Width	100, **200** and 400	km
Step Material Proportion	$\frac{2}{3}$ Cont., **Equal** and $\frac{2}{3}$ Oce.	–

Viscosity				
Profile[a]	Minimum viscosity μ^0_{min} (Pa s)	Channel	Activation volume V_1^*, V_2^* ($m^3\,mol^{-1}$)[b]	Pre-factor A_1, A_2 (Pa s)[b]
	$\mathbf{10^{19}}$	**No**	$\mathbf{6.8 \times 10^{-6}}$	$\mathbf{1.9 \times 10^{-8}}$
	10^{19}	Yes	25×10^{-6}, 3×10^{-6}	2.1×10^{-6}, 2.1×10^{-10}
	10^{20}	No	4.7×10^{-6}	1.1×10^{-9}
	10^{20}	Yes	25×10^{-6}, 3×10^{-6}	2×10^{-7}, 2.1×10^{-10}

Others		
Name	Values	Units
Velocity Inflow	Figure 1b and Equation 7	–
Water Content	200, **300**, 500 and 1000	ppm

Note. Reference case values are in bold.

[a] Refer to Figure 1a for visualization of the profiles.

[b] In the absence of a channel, activation volumes and pre-factors are identical in both laws (Equation 3).

static pressure condition. Each profile includes, and differs from the others by, a constant velocity, u_{plate}, in the lithosphere and a Poiseuille component in the sub-lithospheric mantle, down to $z_{pois} \equiv 200$ km depth (Höink & Lenardic, 2010; Höink et al., 2011; Stotz et al., 2018; Rolf et al., 2018). We evaluate the latter according to

$$u_{pois} = u_{plate} \times \left(1 + \frac{1}{2}\frac{z - z_{oce}}{z_{pois} - z_{oce}}\left(1 - \frac{z - z_{oce}}{z_{pois} - z_{oce}}\right)\right), \tag{7}$$

for which z_{oce} is the initial thickness of the oceanic lithosphere. A linear decrease across the remainder of the upper mantle, with no inflow permitted in the lower mantle, completes the imposed profile. We couple the change in kinematic boundary condition at $x = 0$ km to a Dirichlet condition on the temperature, using the initial thermal structure of the oceanic lithosphere, and we shift the continent to the left of the domain, between 1000 km and 2500 km, to provide enough space for advection.

2.3.2 3-D Cases

We extend our analyses to 3-D to quantify the sensitivity of EDC and SDU to more complex continental geometries and a broader spectrum of orientations for background mantle flow, relative to the continent. We keep the remaining model parameters identical to our reference 2-D case.

We examine four continental geometries for which the shape of the continent is based on a 200 km thick cuboid located between x = 1750 km, y = 1250 km and x = 3250 km, y = 2750 km (Figure 2). Similarly to 2-D, lithospheric steps connect continent to ocean along continental boundaries, including the four 'corners'. Each case differs in the following way: (i) Case U400 incorporates a 400 km wide indent inside the continent, be-

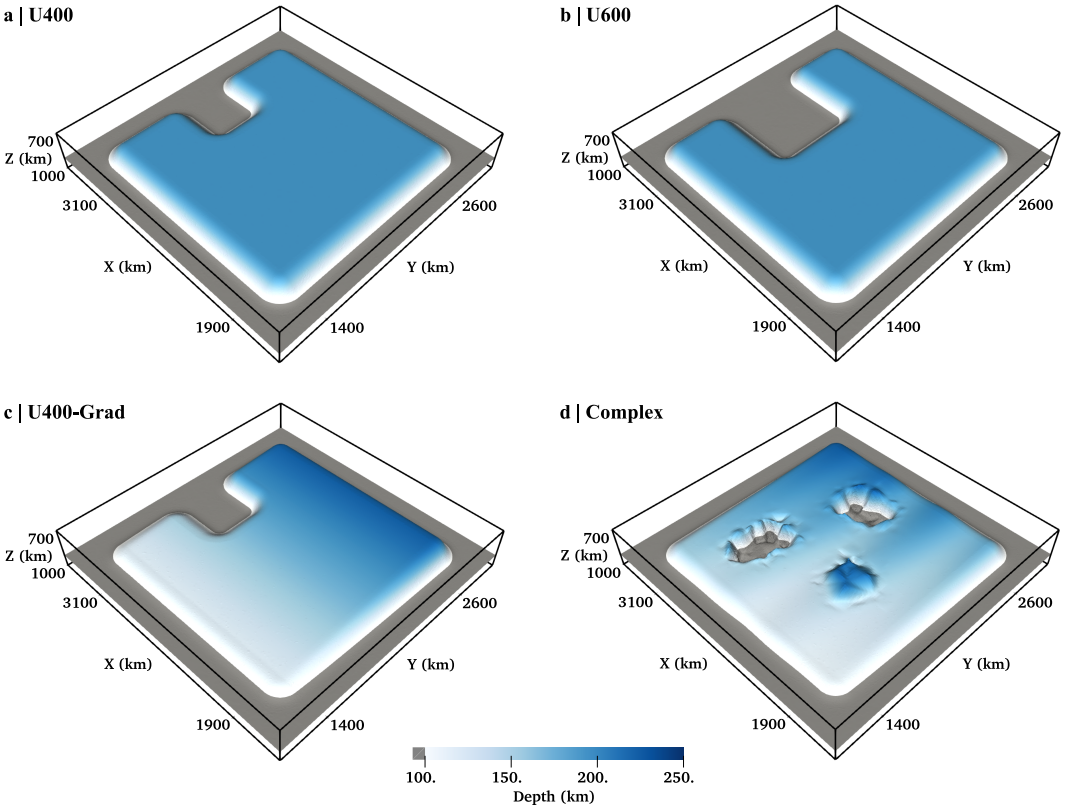

Figure 2. Initial topography at the LAB, as given by the 1620 K isotherm proxy, for continental geometries used in the 3-D simulations. (a) Case U400. (b) Case U600. (c) Case U400-Grad. (d) Case Complex.

tween x = 2850 km, y = 1800 km and x = 3250 km, y = 2200 km, which effectively replaces continental lithosphere by oceanic lithosphere, with additional steps at inner edges and corners accounting for the new boundary; (ii) Case U600 is similar to Case U400, albeit with a wider indent of 600 km, located between x = 2650 km, y = 1700 km and x = 3250 km, y = 2300 km; (iii) Case U400-Grad builds on Case U400 but differs by the presence of a linear gradient in the y-direction, from z = 130 km to z = 230 km depth, to represent the continental LAB; (iv) Case Complex does not incorporate an indent but, instead, combines a similar gradient as Case U400-Grad (same direction, different amplitude) with sinusoidal variations and local anomalies to define the continental LAB. These smaller-scale variations in LAB topography are more consistent with the LAB inferred through seismic techniques and probabilistic inversion of multiple datasets (e.g. Afonso et al., 2016; Rawlinson et al., 2017), and allow us to investigate the flow regime and melt patterns in a more complex scenario.

To explore the effects of background mantle flow, we select Case U400 as our basis and apply our 4 cm yr^{-1} inflow profile (Section 2.3.1 and Figure 1b) in four different directions: positive x at $x = 0$ km, negative x at $x = 5000$ km, positive y at $y = 0$ km and both positive x and y (which we will refer to as oblique) at $x = 0$ km and $y = 0$ km. For the latter, we also apply the inflow profile at the outflow boundaries to ensure the flow remains oblique inside the domain. As for 2-D cases, we shift the continent toward the inflow boundary, at a distance of 1000 km.

2.4 Model Diagnostics

For our 2-D cases, we identify the edge-driven cell generated adjacent to the step in lithospheric thickness and quantify its strength. In the presence of imposed background flow, we uncover the cell by subtracting from the velocity field a vertical profile of u_x, representative of continental motion. Following Coltice et al. (2018), we calculate at each mesh node the angle of the velocity vector relative to the x-axis and the horizontal derivative of the vertical component of velocity, $\frac{\partial u_z}{\partial x}$. Then, we tessellate the domain using large squares, inside which we analyse angle and derivative values. For a cell to exist, velocity vectors must be oriented such that they form the shape of an ellipse. Accordingly, we require the equivalent condition that vector directions distribute in all four quadrants of the unit circle, which we interpret in terms of the distribution of angles. Moreover, we apply a threshold to the absolute value of the derivative (e.g. $3 \times 10^{-15}\,\mathrm{s}^{-1}$ for the reference viscosity profile), filtering out squares with only low-intensity features. We test each square for both conditions and either discard those that do not meet our criteria or decompose others into four sub-squares. We iterate through the process until a minimum threshold for the size of the squares is reached (e.g. 10 km sides, depending mainly on the achievable velocity field resolution). At this stage, we consider the remaining squares to contain the centre of a cell, approximately defined by the square's centroid. With the centre of each cell known, relevant velocity profiles can be drawn and compared across multiple cases.

We monitor melting using recently implemented Lagrangian tracer particles in Fluidity. We calculate weight fractions of melt, F, using the batch melting parameterization for wet, shallow upper-mantle peridotite from Katz et al. (2003), which addresses both the exhaustion of clinopyroxene and water saturation in the rock. Our implementation considers the pressure to be lithostatic, incorporates the adiabatic temperature increase with depth (consistent with our viscosity formulation) and makes use of an algorithm for root-finding (Brent, 2013). Each Lagrangian particle records a value of F at each time-step and stores the maximum value encountered throughout the simulation, F_{max}. We consider melting to occur when the newly obtained F is higher than F_{max} and a melting rate, M, is subsequently calculated based upon the value of the time-step, δt, at this stage:

$$M = max\left(0, \frac{F - F_{max}}{\delta t}\right). \tag{8}$$

Neither melt extraction nor melt 're-freezing' are considered. Particles are randomly initialised within a cuboid that extends 500 km beyond the continent in horizontal direction(s), and down to 450 km depth; we use 10^5 and 1.5×10^7 particles in 2-D and 3-D simulations, respectively. At the beginning of the simulation ($t = 0$), F is calculated according to the pressure and temperature conditions of the initial state, with F_{max} updated accordingly; we set M to 0.

For all simulations, we calculate the cumulative melt production beneath a region of interest, surrounding the continent. To do so, at each time-step, we select particles within a given depth range where melting is occurring (e.g. between 30 km and 140 km) and construct a piecewise linear interpolant from the obtained melting rate. We then apply the interpolant onto a 5 km-resolution structured grid and use Simpson's rule to integrate along any space dimension, as well as multiply by the current model time-step to integrate in time. We obtain cumulative melt thicknesses/areas/volumes by summing results from each time-step. To account for continental motion in cases with a prescribed inflow, we advect the grid according to the motion of a particle that is located within the rigid continent. Throughout the algorithm, we discard the initial state and the first time-step (< 0.1 Myr) as we consider them to represent an equilibrium process between the initially unmolten rocks and the pressure-temperature-velocity conditions of the model.

3 Results

3.1 Two-Dimensional Simulations

We first examine results from our 2-D simulations. Our reference case incorporates 40 Myr old oceanic lithosphere, a 200 km thick continent and 200 km wide steps, with the material interface between continent and ocean halfway along the step. The initial viscosity distribution reaches a minimum of 10^{19} Pa s in the sub-lithospheric oceanic mantle and does not include a low-viscosity channel; domain boundaries are closed. We focus on the dynamics around the right step, for which Figure 3 illustrates the first 30 Myr of model evolution. A cell-like flow develops, adjacent to the lithospheric step. Flow rapidly expands and intensifies, with peak velocities rising from a few mm yr^{-1} after 7 Myr to greater than 1 cm yr^{-1} after 15 Myr. Motion is driven by the negative buoyancy of oceanic material at the step. Continental lithosphere, owing to its lower density and increased viscosity, acts as a steady, rigid block, and guides downward motion; corresponding upwelling flow occurs beneath adjacent oceanic lithosphere. A secondary instability initiates away from the step after $\sim$15 Myr. Melting occurs where upwelling material impinges beneath oceanic lithosphere, leading to melting rates of, on average, a few 100 ppm Myr^{-1}, with some particles recording $\sim$1 ‰ Myr^{-1}; melt fractions reach a maximum value of

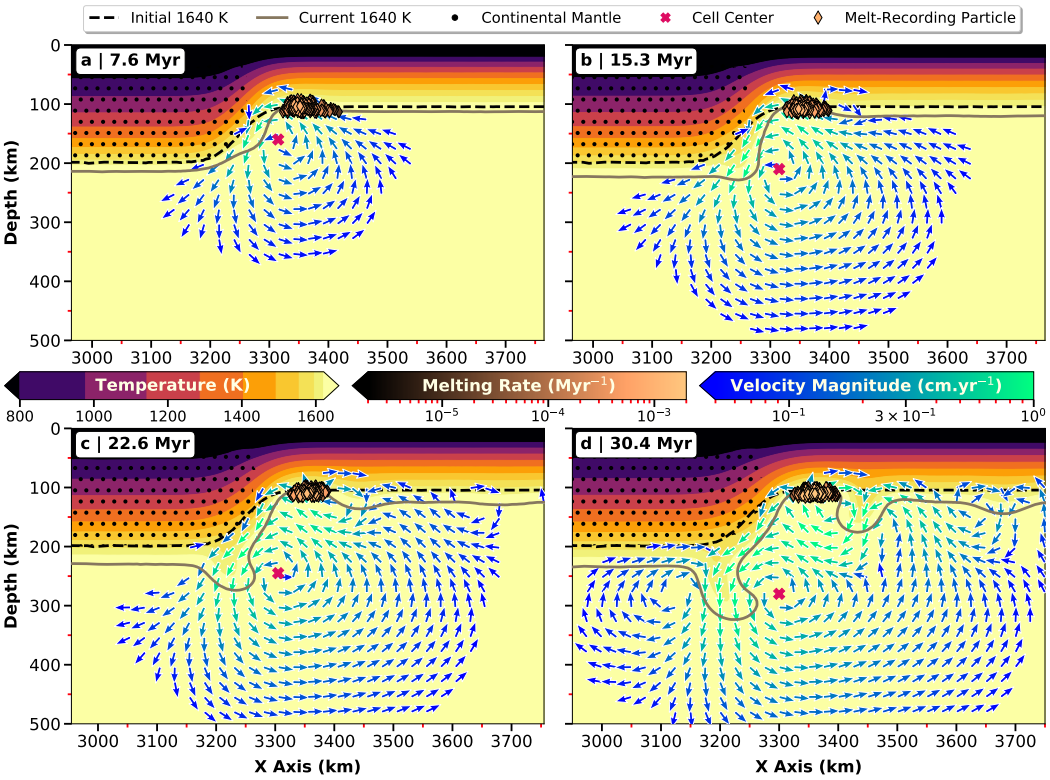

Figure 3. Development of an instability adjacent to the right step of the reference 2-D case. Background colours represent temperature, with the current and initial location of the 1640 K isotherm – a convenient proxy for downwellings – highlighted by the solid grey and dashed black line. Black dots depict the location of continental mantle. Arrow glyphs illustrate the intense part of the velocity field, where the magnitude is higher than 0.5 mm yr^{-1}, and their colour indicates the strength of the flow. The pink cross denotes the centre of the cell while small diamonds, coloured by melting rate, represent particles that record active melting.

0.6 %. Melting is initially induced by the main edge-driven flow and subsequently enhanced by the secondary instability, which delays lithospheric thickening and can locally enhance upwelling flow.

We next examine the role of background mantle flow, using our 4 cm yr^{-1} velocity inflow profile (Figure 1b, red curve). As illustrated in Figure S1, this background flow dominates the velocity field across the entire upper mantle: although a component of upwelling flow is present adjacent to the step, no clear cell is visible as velocity glyphs strongly align with the prescribed inflow profile. To better illustrate buoyancy-driven flow adjacent to the step, we subtract a vertical profile of horizontal velocity, which is representative of continental motion, from the whole field, revealing a cell adjacent to the step (Figure 4). Both the primary instability at the continental edge and associated upwelling flow within this cell are enhanced compared to our reference case, with vertical velocities and stronger upward motion extending deeper into the domain. The asthenospheric shear associated with the prescribed inflow, however, delays the onset of secondary instabilities. Consequently, melting initially occurs over a larger horizontal length scale, in comparison to the reference case, and is of slightly higher intensity, as depicted by increased melting rates, particularly for the first ∼20 Myr of the simulation (Figure S4). However, the absence of secondary instabilities, over the simulation time examined, restricts melting at later stages in comparison to the reference case.

We now compare the vigour of edge-driven instabilities across the parameter space investigated. For each case, we plot a horizontal profile of vertical velocity, centred on the cell, at the right lithospheric step (Figure 5). As instabilities develop on different time-

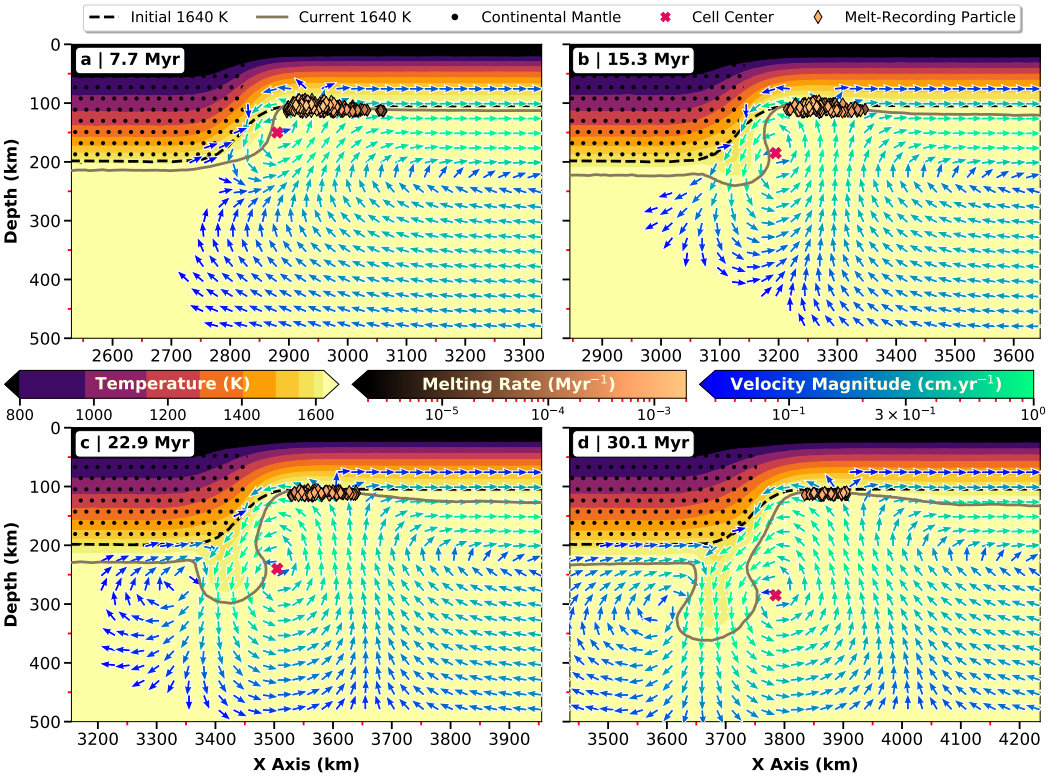

Figure 4. Evolution of our 4 cm yr^{-1} inflow profile case over 30 Myr. A vertical profile of horizontal velocity, representative of continental motion, is subtracted to the whole field to uncover the cell flow. Graphic illustration is similar to Figure 3.

scales for different cases, to provide a meaningful comparison across our parameter space, we identify the centre of the cell in each simulation (Figure S3) at the time of maximum downwelling velocity (Figure S2), prior to the onset of secondary instabilities.

As illustrated in Figure 5a, geometric parameters generally have only a moderate influence on the downwelling velocity, upwelling velocity and cell width (i.e. the distance between maximum downwelling and upwelling velocities along the profile) over the parameter space examined. The case with a thinner continent, however, stands out: in comparison to the reference case (compare '140 km Cont.' to 'Reference'), the cell is smaller in both its depth and lateral extent, with peak downwelling velocities reduced but peak upwelling velocities enhanced. Reduced downwelling velocities are a consequence of the smaller extent of the continental guide at depth and a more stable step relative to the reference case, both of which lead to a less voluminous downwelling. The conservation equations imply that the corresponding upwelling should also be less voluminous, which is the case, although peak upwelling velocities are larger (but drop off more rapidly with distance from the cell centre). This is a long-term consequence of weaker horizontal return flow beneath oceanic lithosphere: weaker shearing occurs beneath the LAB because less material is being displaced at the step, thus promoting the earlier development of secondary instabilities, which can locally boost upwelling velocities (particularly at later

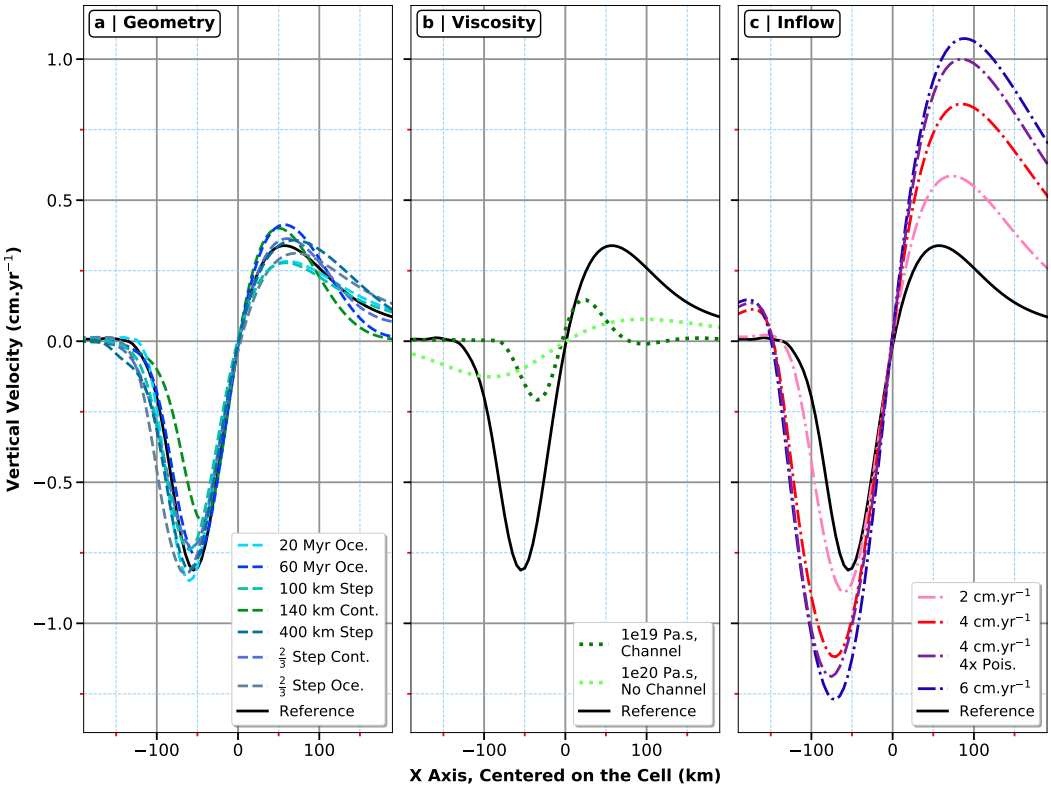

Figure 5. Comparison of vertical velocity in the vicinity of the cell centre (Figure S3) for the 2-D simulations examined herein, at the time of maximum downwelling velocity (Figure S2). Each profile represents a 300 km horizontal transect passing through the centre of the cell. (a) Effect of step geometry – 'Reference' corresponds to 40 Myr Oce., 200 km Step, 200 km Cont., and a material boundary halfway along the step. (b) Role of viscosity – 'Reference' corresponds to a channel-free profile with a minimum viscosity of 10^{19} Pa s. (c) Influence of background mantle flow – 'Reference' corresponds to an enclosed simulation.

stages of the simulation). Similarly, the case with older oceanic lithosphere ('60 Myr Oce.') also exhibits a weaker downwelling and a more focussed upwelling. Here, weaker downwelling can once again be attributed to a smaller continental guide, albeit on this occasion resulting from thicker oceanic lithosphere, which reduces the build up of negative buoyancy at the step. The more focussed corresponding upwelling can be attributed to secondary instabilities, which develop more rapidly beneath older oceanic lithosphere. Differences for the remaining cases, when compared to the reference model, can be understood based on the initial buoyancy of oceanic lithosphere and the position and orientation of the material interface along the step, which determine the relative proportion of step material that can become unstable. Nevertheless, trends are generally closely matched, with the main difference induced by these geometrical parameters being the time required for instabilities to fully develop (Figure S2).

In Figure 5b, we illustrate the role of the viscosity profile, particularly the effect of the minimum value in the sub-lithospheric mantle and the presence of a low-viscosity channel. At a minimum viscosity of 10^{19} Pa s, the presence of a low-viscosity channel stabilizes the lithosphere, as increased momentum diffusion occurs at shallower depths, leaving less vertical space for the instability to develop. The cell width and flow intensity are greatly reduced, as the cell center is pushed upward (Figure S3). Increasing the minimum viscosity to 10^{20} Pa s changes the dynamics of the model: no comparable cell forms, as the higher viscosity restricts the development of any clear downwelling at the lithospheric step over the simulation times examined. Adding a low-viscosity channel further inhibits the development of an edge-driven cell.

Figure 5c combines results from cases where a velocity inflow is prescribed and highlights that the presence of favourable background mantle flow (i.e. where the underlying mantle flows away from the continent) strongly enhances vertical velocities adjacent to the step. Moreover, additional asthenospheric shear, provided via an enhanced Poiseuille component (Figure 1b, compare violet and red profiles), leads to a slight increase in both downwelling and upwelling velocities, and a marginal increase in cell width.

We finally discuss the melt-related diagnostics for our 2-D simulations. To allow for a quantitative comparison between different cases, we define a 5 km resolution grid surrounding the continent onto which we interpolate melting rates recorded by the particles. The grid extends 350 km away from the centre of the steps, between depths of 30 km and 140 km; for cases with prescribed inflow, we advect the grid using the evolution of position from a particle trapped inside the continent. We subsequently integrate the interpolated melting rates in both space and time to determine the cumulative amount of melt produced at a given time, with results presented in Figure 6. In comparison to Figure 5, we include an additional panel that illustrates the effect of variable water content (we emphasise that, in our models, water only influences the melt production, without any feedback on the flow dynamics). To complement the cumulative melting results presented, instantaneous melting rates, integrated over the same area, are illustrated in Figure S4. Figure 6a demonstrates that most alternative geometries generate slightly less melt than the reference case after 30 Myr. However, younger (thinner) oceanic lithosphere promotes an increase in decompression melting, whilst older (thicker) oceanic lithosphere inhibits melting through a thick lid. Focussing next on Figure 6b, cases with a minimum viscosity of 10^{20} Pa s exhibit only extremely limited melting, which is not visible on the scale plotted. At 10^{19} Pa s, the incorporation of a channel reduces by a factor of four the cumulative amount of melt, as expected from the decreased upwelling velocities highlighted in Figure 5b. Figure 6c demonstrates that background flow enhances melt production, with the melting rate proportional to the prescribed velocity. After 20 Myr, however, cumulative melt production trends for cases with background flow start to flatten, due to the fact that instantaneous melting rates drop, eventually falling below those recorded in the reference case (Figure S4c). Such a decrease is a direct consequence of the delayed onset of secondary instabilities in oceanic lithosphere, for cases with substantial astheno-

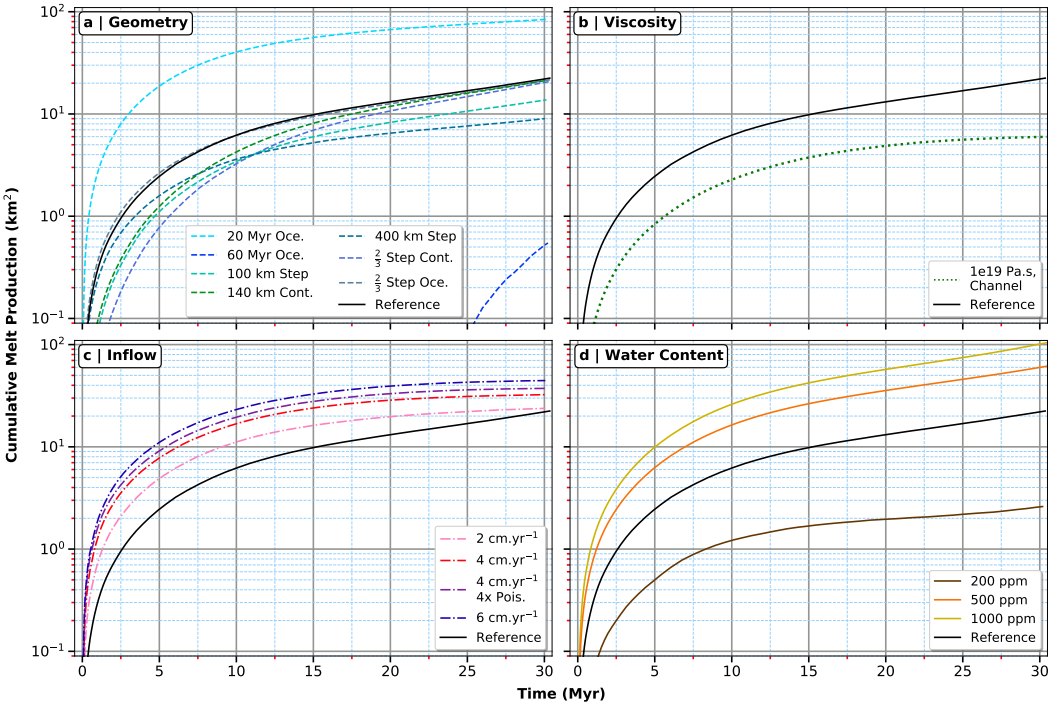

Figure 6. Cumulative melt production as a function of time, sampled at the right step. Values correspond to the integral in both space and time of interpolated melting rates as recorded by particles, summed at each time-step. (a) Effect of step geometry – 'Reference' corresponds to 40 Myr Oce., 200 km Step, 200 km Cont., and a material boundary halfway along the step. (b) Role of viscosity – 'Reference' corresponds to a channel-free profile with a minimum viscosity of 10^{19} Pa s. (c) Influence of background mantle flow – 'Reference' corresponds to an enclosed simulation. (d) Impact of water content – 'Reference' corresponds to 300 ppm.

spheric shear (e.g. van Hunen et al., 2003; Le Voci et al., 2014; Davies et al., 2016). It is worth noting that the 2 cm yr^{-1} inflow case eventually yields instantaneous melting rates that exceed those in cases with faster velocities. Finally, as expected, Figure 6d confirms that higher water concentrations enhance melt production.

The melting behaviour described at the right step is comparable to that at the left step, except for cases with prescribed inflow, where imposed velocities reduce both instantaneous and cumulative melting rates (not shown). This indicates the importance of the velocity field orientation with respect to the step in controlling the flow regime and associated melt production, which we further examine in our 3-D simulations.

3.2 Three-Dimensional Simulations

We extend our analyses to 3-D, allowing for the incorporation of more complex geometries and greater flexibility in the orientation of background mantle flow. We separate our results into cases that neglect (Section 3.2.1) or incorporate (Section 3.2.2) background mantle flow, respectively.

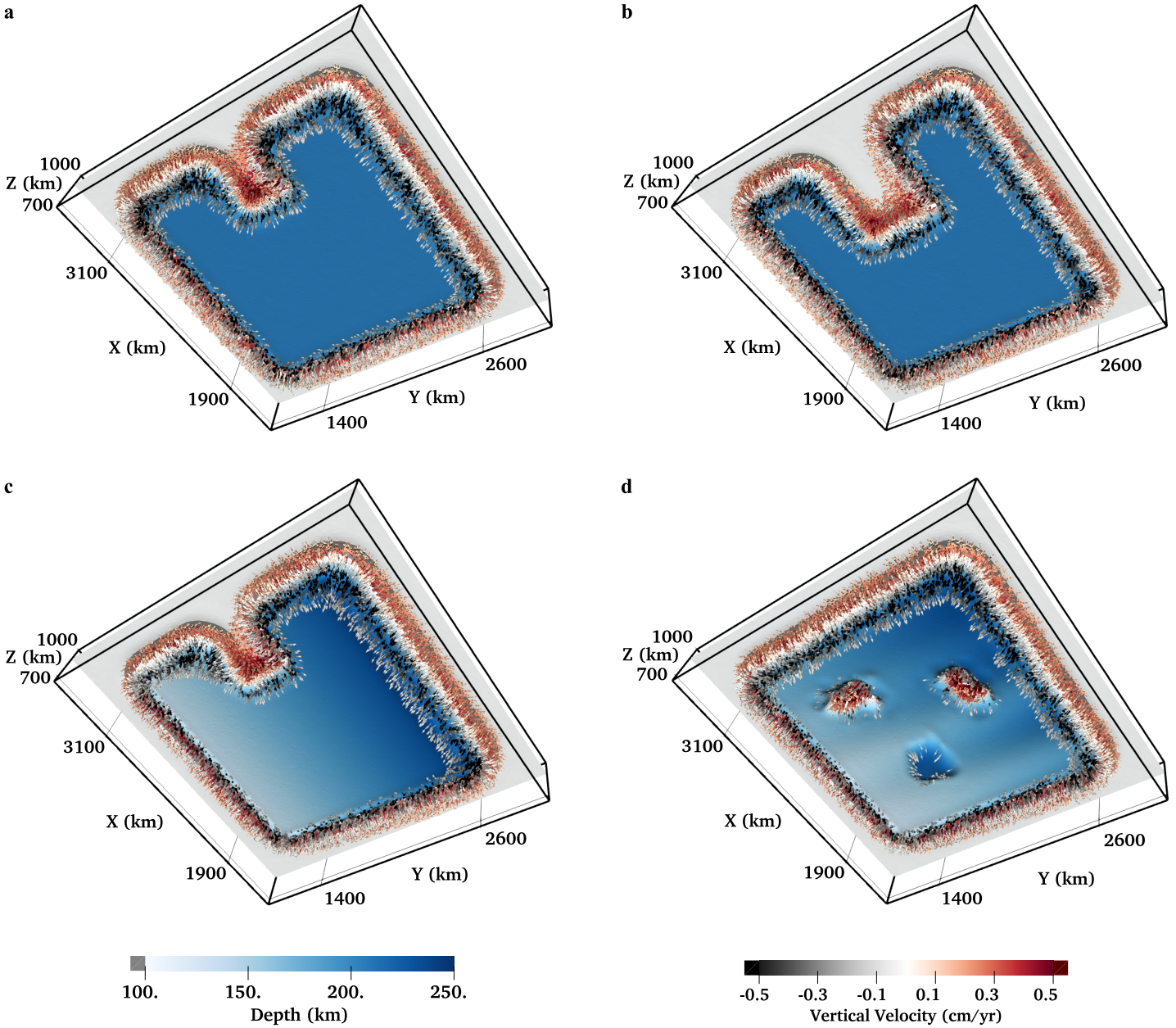

Figure 7. Three-dimensional representation of the velocity field around the continent at 15 Myr. Surface colours correspond to the depth of the 1620 K isotherm – our proxy for lithospheric thickness – while arrow glyphs illustrate the velocity field. For visualization purposes, glyphs are only drawn at locations where the velocity magnitude is larger than 2 mm yr^{-1}; glyphs all have the same length, are evenly distributed and are coloured according to the velocity vertical component. (a) Case U400. (b) Case U600. (c) Case U400-Grad. (d) Case Complex.

manuscript submitted to *Geochemistry, Geophysics, Geosystems*

3.2.1 No Prescribed Background Flow

We first examine the velocity field generated after 15 Myr. This is sufficient to allow for the development of primary instabilities at lithospheric steps, whilst also avoiding complications linked to the onset of secondary instabilities, enabling us to focus upon 3-D effects that arise from more complex continental geometries. Nonetheless, we illustrate, through Figure S8 (which is directly comparable to Figure 2), the effect of secondary instability development after 30 Myr on all 3-D geometries examined. Figure 7a illustrates the flow regime for Case U400, which exhibits edge-driven instabilities adjacent to the entire continental boundary. Consistently with our 2-D cases, these instabilities are driven by unstable oceanic lithosphere, sinking at the continental edge, with a corresponding passive upwelling forming beneath adjacent oceanic lithosphere. Around the continent, velocities are of comparable intensity, except within the indent, where darker red glyphs denote more vigorous upwelling. At this location, the geometry of the interface between ocean and continent brings upwelling flows associated with three adjacent steps into close proximity. These coalesce (Figure S6a) to enhance upwelling velocities by up to 70 % compared to those in other parts of the domain (Table 3).

Figure 7b displays comparable flow patterns for Case U600. Although similar high-intensity upwelling velocities are present inside the indent, they are restricted to the internal corners. In this case, the distance between edge-driven cells exceeds the width of the cells and, accordingly, cells on opposing steps are unable to coalesce and influence each other to the same extent as in Case U400 (Figure S6b). Figure 7c illustrates results from Case U400-Grad, with a complementary cross-section presented in Figure S7. Similar to the observations made from Figure 5a, downwelling velocities are enhanced adjacent to thicker parts of the continent. This gives rise to more intense horizontal motion at depth, resulting in broader edge-driven cells and more shearing immediately beneath the oceanic LAB, deflecting upwelling flow. Accordingly, despite enhanced downwelling velocities on steps adjacent to thicker continents, peak upwelling velocities are generally comparable to those on shorter steps, which are modulated through the action of secondary instabilities (in agreement with Figure 5a). Figure 7d illustrates flow pat-

Table 3. *Diagnostics Across 3-D Models*

Case	Maximum downwelling inside | outside indent ($cm\,yr^{-1}$)	Maximum upwelling inside | outside indent ($cm\,yr^{-1}$)	Maximum melt[a] inside | outside indent (km)	Indent's corner melt[b] volume[c] (km^3) & area[d] (km^2)
U400	−1.08 | −1.08	0.70 | 0.41	0.59 | 0.23	3410 & 14,611
U600	−1.10 | −1.10	0.66 | 0.41	0.59 | 0.24	3426 & 14,678
U400-Grad	−1.07 | −1.13	0.64 | 0.49	0.57 | 0.23	3394 & 14,911
Complex[e]	−0.60 | −1.14	0.89 | 0.49	0.88 | 0.24	3936 & 15,256
Pos. x	−1.06 | −1.27	1.09 | 0.70	0.67 | 0.32	4820 & 17,033
Neg. x	−1.10 | −1.30	0.44 | 0.74	0.29 | 0.33	1357 & 9544
Pos. y	−1.25 | −1.31	0.95 | 0.71	0.62 | 0.32	4511 & 16,778
Oblique	−1.09 | −1.40	1.12 | 0.65	0.70 | 0.28	5403 & 17,722

[a] Cumulative thickness over the first 15 Myr of model evolution obtained by integration of the melting rate carried by particles both in time and along the vertical axis. [b] Nodes (Section 2.4) with a cumulative melt production greater than 0.05 km (Figures 8 and 10) that are closest to the bottom-left inner corner of the indent (black square in Figure 8a). [c] Integration of the cumulative thickness (Figures 8 and 10) in both x and y directions. [d] Corresponding area experiencing melting. [e] For the first three columns, 'inside | outside the indent' is swapped for 'inside | outside the continent', while the last column 'indent's corner' is replaced by 'right trough' (black rectangle in Figure 8d).

terns for Case Complex and clearly demonstrates that regions of anomalously thin continental thickness are associated with localised and vigorous upwelling flows. However, no downwellings are visible adjacent to the anomalously thick continental region, which is a consequence of the higher viscosity of continental material. Instabilities along continental boundaries are consistent with those in Case U400-Grad, as expected.

We now analyse the cumulative melt production for these four cases. Results, presented in Figure 8, are expressed as a thickness, which results from the integration of the melting rate both in time (over 15 Myr) and along the vertical axis (Section 2.4). Most

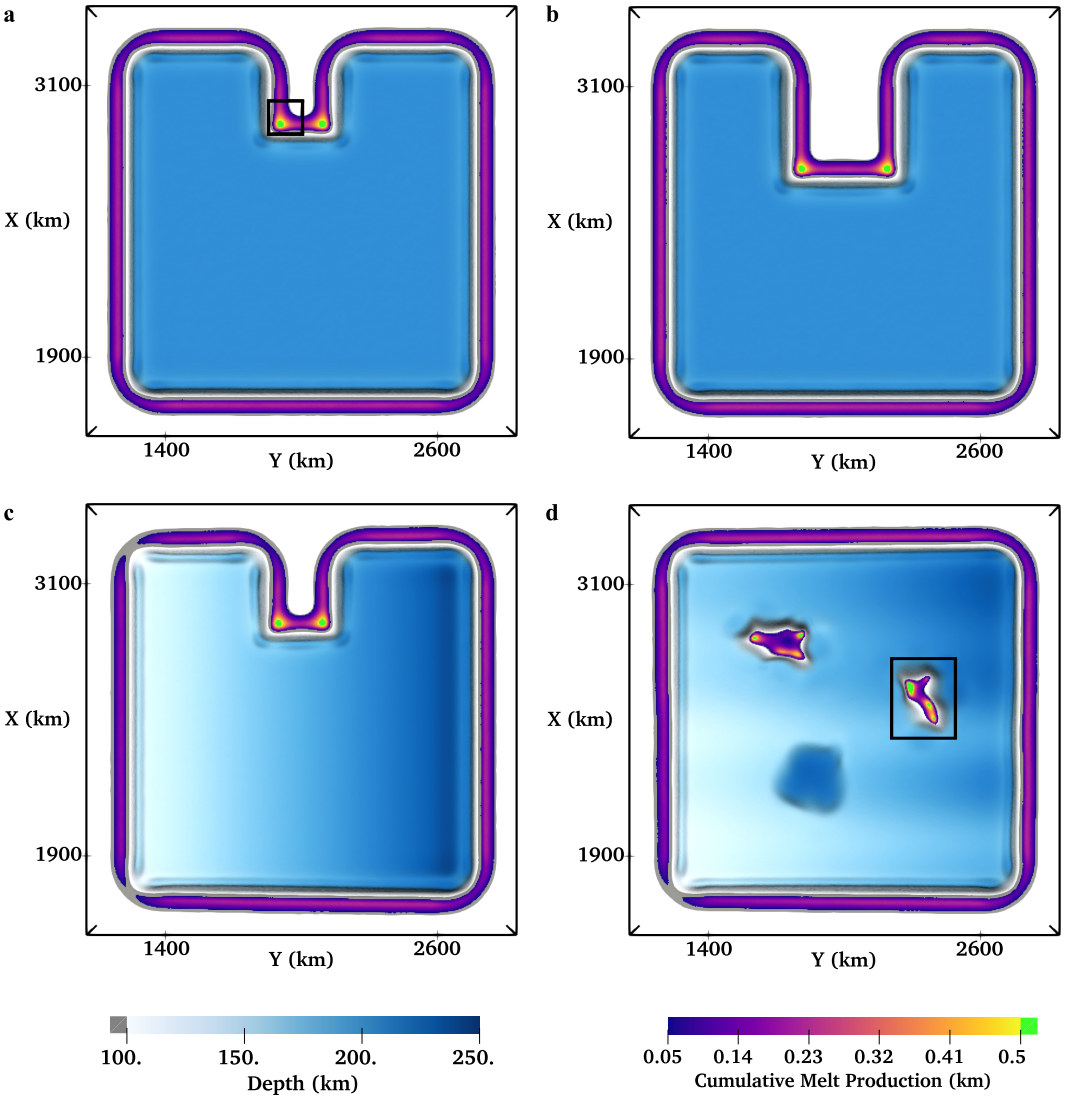

Figure 8. Distribution and intensity of the cumulative melt production around the continent for cases without prescribed inflow, after 15 Myr. Surface colours correspond to the depth of the 1620 K isotherm, our proxy for lithospheric depth; lithospheric erosion is identified by the grey tone, which depicts portions thinner than 100 km. Coloured points represent the cumulative melt production as obtained after integration along the vertical axis (Section 2.4); major locations of melting are indicated by the green tone. Black rectangles illustrate zones of interest used for calculations in Table 3. (a) Case U400. (b) Case U600. (c) Case U400-Grad. (d) Case Complex.

melting occurs between 90 km and 120 km depth, consistent with the 2-D cases, except where the lithosphere is sufficiently thin to host shallower melting. For Case U400, illustrated in Figure 8a, we observe three distinct melting trends: (i) weak melting, less than $\sim$0.15 km, adjacent to the external corners of the continent; (ii) moderate melting, up to $\sim$0.25 km, at external steps, away from the corners, that is homogeneous throughout; and (iii) enhanced melting, up to $\sim$0.6 km, within the indent, with the largest melting concentrated at the indent's internal corners. Within the indent's lower-left corner, additional horizontal integration yields a cumulative volume of $\sim$3400 km^3, distributed over an area of $\sim$14,500 km^2 (Table 3); individual melt fractions reach a value of 1 %. These trends are fully consistent with the intensity of upwelling flow at these locations.

In Figure 8b, we illustrate results for Case U600. Similar trends to Case U400 are displayed; despite weaker coalescence of flow within the indent (Figure S6), the geometry of the internal corners triggers melting that is comparable to that yielded by a narrower indent. For Case U400-Grad (Figure 8c), steps adjacent to thicker parts of the continent generate around 15 % more melt than those adjacent to thinner parts, with a gradient in between. Even though such disparity seems to contradict the comparable upwelling velocities observed in Figure 7c, it is in agreement with the 2-D results shown in Figure S4a (compare the evolution of '140 km Cont.' to 'Reference') and can be reconciled based on the faster development of secondary instabilities adjacent to smaller steps. As demonstrated in our 2-D cases, during the first 15 Myr of model evolution, peak upwelling velocities are generally smaller for cells adjacent to shorter steps, leading to the lower melt production observed. However, the faster onset of secondary instabilities adjacent to these steps can enhance upwelling velocities and, thereby, melting rates at later times, relative to those adjacent to thicker steps. Finally, for Case Complex (Figure 8d), trends at external steps are consistent with case U400-Grad. Within the continent, significant melting is restricted to the two anomalous troughs, coincident with the vigorous upwellings highlighted in Figure 7d. As a result of the initially thin continental lithosphere at these locations (reaching a maximum thickness of 60 km in places, as opposed to 90 km for surrounding oceanic lithosphere), we record up to 0.9 km of cumulative melt production, which is 50 % higher than observed adjacent to the indent's internal corners in Case U400.

3.2.2 Prescribed Background Flow

We next examine cases that incorporate prescribed background mantle flow and focus on how its orientation, relative to the continent, affects dynamical instabilities throughout the domain. We use Case U400 as our reference and systematically prescribe flow in the positive x, negative x, positive y and both positive x and y (oblique) directions. Similarly to the enclosed models, we illustrate our results initially through the flow field (Figure 9) and, subsequently, through its influence on melting (Figures 10 and 11).

When visualising the flow field, we find that glyphs principally align with the prescribed inflow direction, consistent with the behaviour observed in 2-D (Figure S1). Therefore, to better highlight instabilities driven by buoyancy, and to allow for consistent comparison with our 2-D cases, we remove a vertical profile of horizontal velocity, characteristic of continental motion, from the velocity field. Figure 9a illustrates the resulting flow in the case of inflow in the positive x-direction. In comparison to Case U400 (Figure 7a), for which there is no background flow, we observe enhanced upwelling velocities where the asthenosphere flows away from the continent (i.e. the trailing edge), increasing by up to 55 % inside the indent and 70 % elsewhere. Conversely, where the asthenosphere flows toward the continent (i.e. the leading edge), upwelling velocities are reduced substantially, by 75 %. The leading edge exhibits a clear downwelling, with no associated upwelling, as well as a divergent flow adjacent to the corners, while the trailing edge displays intense upwelling motion, with convergent flow at the corners. The flow field adjacent to the continent's external corners is a consequence of the higher pressure

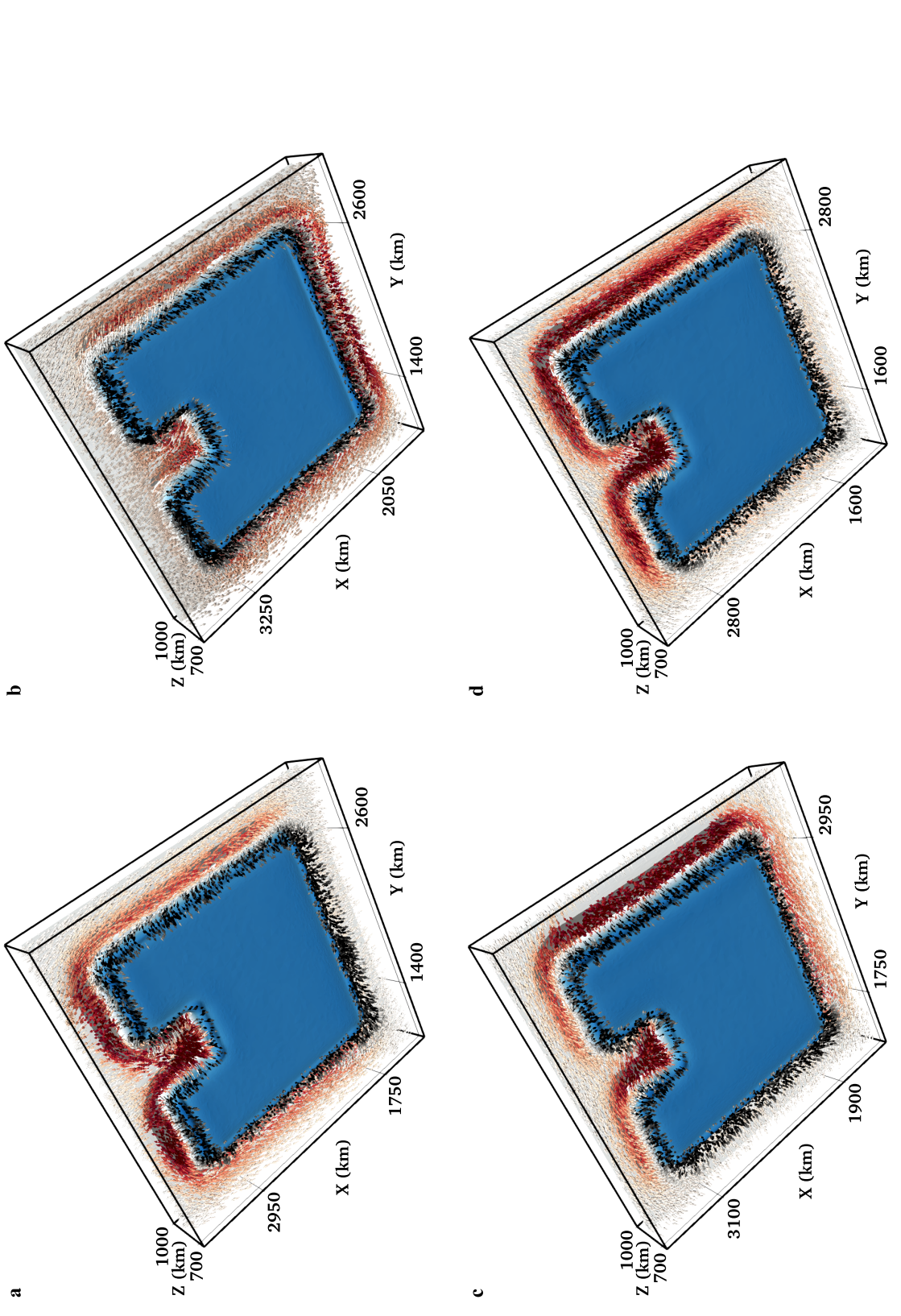

Figure 9. Three-dimensional representation of the velocity field around the continental area after 15 Myr. Graphic illustration is similar to Figure 7; glyphs are only drawn where the velocity magnitude is greater than 4 mm yr^{-1}. Similarly to Figure 4, a vertical profile of horizontal velocity, aligned with the prescribed inflow and representative of continental motion, is subtracted to the whole field, uncovering dynamical instabilities. (a) Prescribed flow in the direction of positive x. (b) Direction of negative x. (c) Direction of positive y. (d) Direction of both positive x and y.

beneath the continent, which drives material around continental margins and, accordingly, contributes toward upwelling at the continent's lateral edges.

Figure 9b illustrates the flow field resulting from a case with inflow in the negative x-direction (i.e. flow in the opposite direction to that illustrated in Figure 9a). While trends are generally identical to the previous case on leading, trailing and outer lateral steps, we note that upwelling velocities within the indent are no greater than those along the continent's lateral margins, with comparable downwelling velocities (Table 3). Such an orientation of the velocity field, therefore, dampens the dynamics driven by the indent's geometric configuration. In Figure 9c, we illustrate the effect of inflow in the positive y-direction. Both strong upwelling and downwelling velocities are observed within the indent (in comparison to Figure 7a), as the flow first upwells at the inner left step before diving beneath the continent at the inner right step. Figure 9d illustrates results

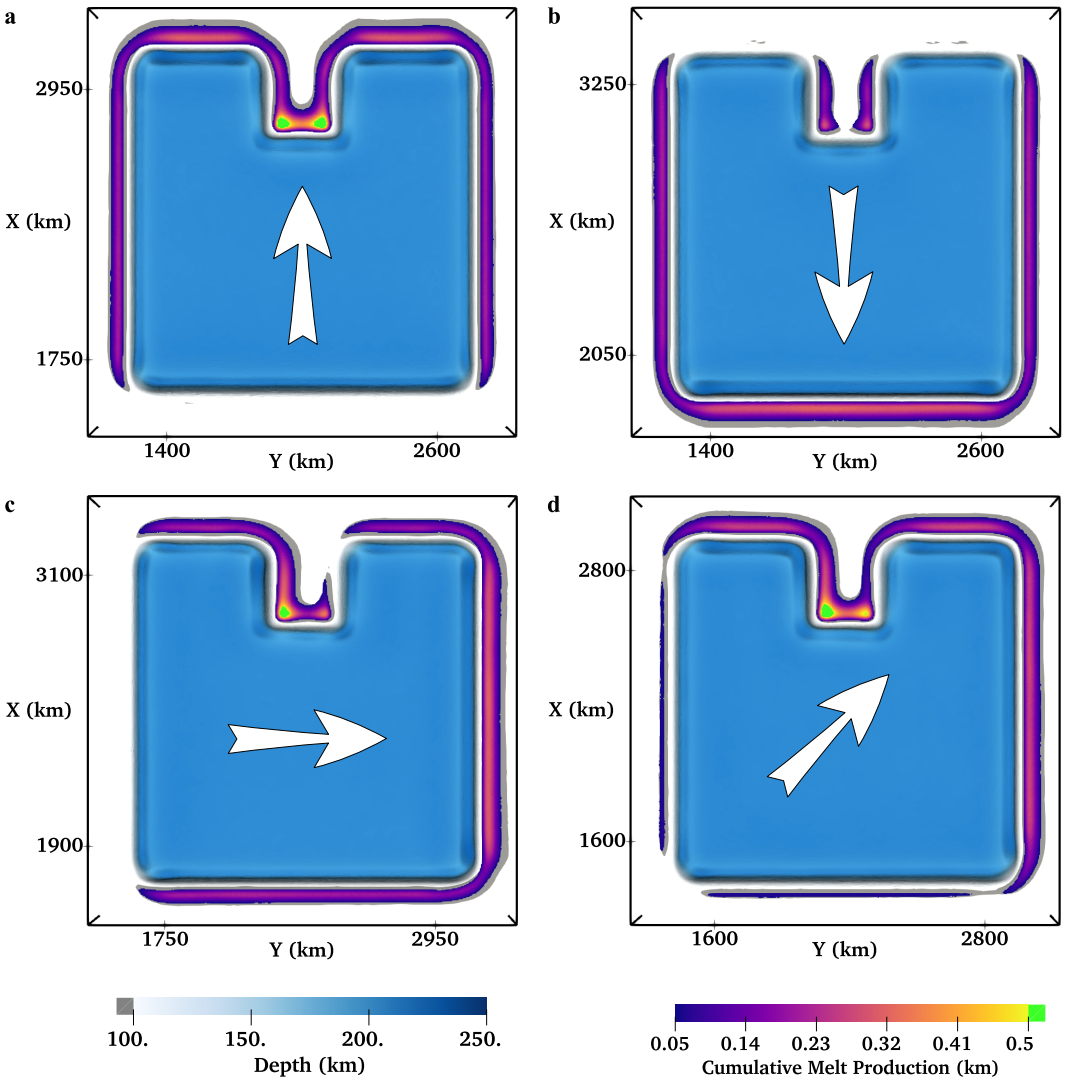

Figure 10. Distribution and intensity of the cumulative melt production around the continent for cases with prescribed inflow, after 15 Myr. Graphic illustration is similar to Figure 8. Additional arrows indicate the direction of the prescribed background flow. (a) Positive x. (b) Negative x. (c) Positive y. (d) Oblique.

from our oblique case, for which the notion of leading and trailing edges evolves into the idea of pairs of edges adjacent to leading and trailing corners. Accordingly, downwellings concentrate alongside the pair of outer edges connected to the leading corner whereas upwellings concentrate adjacent to the opposite edges. The latter are slightly weaker than in the previous three models, although they occupy a longer portion of the continental edge. Within the indent, the lower-left corner and its surroundings experience intense upwelling flow. In this case, the orientation of asthenospheric flow excites two upwellings, on adjacent steps: these enhanced upwellings subsequently interact, yielding the fastest upwelling velocities observed across all cases examined.

As for cases without prescribed background flow, we now link the flow regime to melt production. In Figure 10a, we observe the three trends of melting previously de-

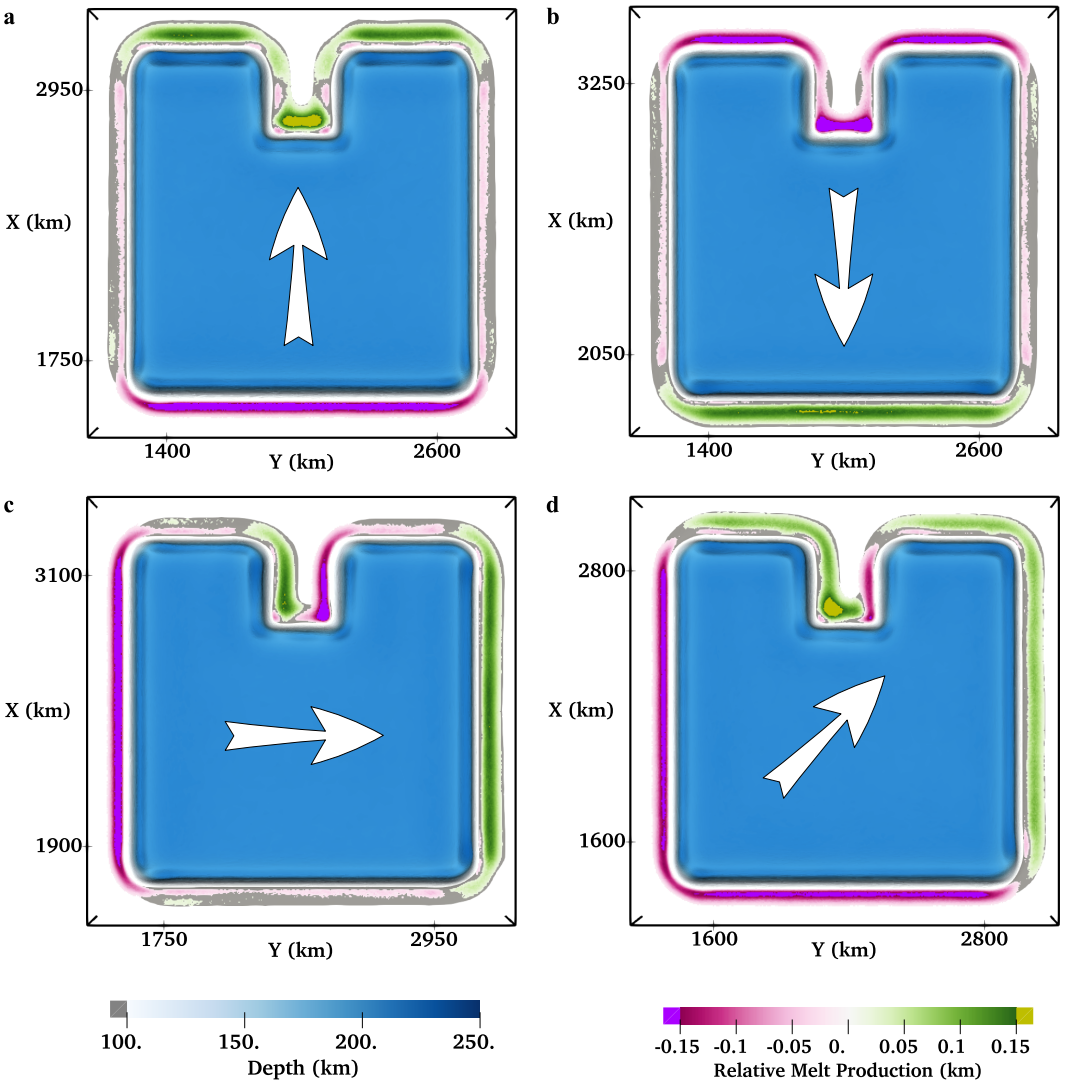

Figure 11. Relative production of melt between cases with prescribed inflow and Case U400. Each panel is generated as a difference between the corresponding panel in Figure 10 and Figure 8a. Pink tones denote areas where melting is weakened by asthenospheric flow, while green tones highlight zones of enhanced melting. Arrows indicate the direction of the prescribed background flow. (a) Positive x. (b) Negative x. (c) Positive y. (d) Oblique.

scribed for our reference 3-D case (Case U400), but, relative to the reference case, melting is absent at the continent's leading edge and enhanced at the trailing edge (by 40 %), in agreement with the velocity field. Nonetheless, despite the substantially enhanced upwelling velocities, the maximum melt production inside the indent only increases by 15 %, relative to Case U400. However, this melting takes place over a larger area than for Case U400, leading to a 40 % increase in local melt volume (Table 3). On Figure 10b, where inflow is prescribed in the opposite direction, similar trends are observed in terms of leading, trailing and lateral edges. In this case, melt production inside the indent is comparable to that observed at the continent's lateral edges and is less than that observed at the trailing edge, which is consistent with expectations from the velocity field (Figure 9b). The calculated melt volume at the indent's lower-left corner falls to $\sim 1350\,\mathrm{km}^3$, which represents a 60 % decrease from Case U400. For inflow in the positive y-direction (Figure 10c), melt production corresponds closely to locations of upwelling flow, especially within the indent. For our oblique case (Figure 10d), melting is absent at the leading external corner and of very low intensity at the pair of adjacent edges. At the opposite edges, melt production is intermediate between a comparable edge that does not experience background flow (e.g. Case U400) and a trailing edge that experiences purely normal flow (e.g. in the case of positive x-inflow). As expected from the velocity field, a large area around the lower-left inner corner of the indent displays intense melt production that is up to 20 % higher than in Case U400. The calculated cumulative melt volume in this region is 60 % higher than Case U400, and is the highest recorded across the parameter space examined.

Finally, we compare the total melt produced in our 3-D cases that incorporate background flow (Figure 10) with Case U400 (Figure 8a). For each panel in Figure 10, we subtract the melt production from Figure 8a, and illustrate the result in the corresponding panel of Figure 11. We make several important observations: (i) the leading edge of a continent is easily identified by a significant decrease in melt production (i.e. $> 0.15\,\mathrm{km}$, dark pink colors) as material descends beneath the continent; (ii) trailing edges display a clear increase in melt production (green tones), as material rises from beneath the continent; (iii) the effect of flow direction is reflected in melting locations within the indent, with melting increasing significantly (i.e. by greater than 0.15 km) where interactions between upwelling currents are facilitated by the geometric configuration; and (iv) melting is displaced outward from lithospheric steps, on both lateral and trailing edges, as a result of background flow.

4 Discussion

In this study, we have quantitatively examined mantle flow in the vicinity of lithospheric steps, under a range of scenarios, using a suite of 2-D and 3-D numerical models. Our motivation was to better understand the dominant controls on edge-driven convection (EDC) and shear-driven upwelling (SDU), as well as potential links to intra-plate volcanism.

In terms of the dynamical flow regime, our results demonstrate that EDC, which is driven by the negative buoyancy of oceanic lithosphere adjacent to rigid continental lithosphere, is strongly sensitive to uppermost mantle viscosity and its depth dependence. At minimum viscosities $\geq 10^{20}\,\mathrm{Pa\,s}$, only weak edge-driven cells develop over the timescales of our simulations. If low viscosities are restricted to a narrow asthenospheric channel, the length-scale and vigour of edge-driven cells are reduced. These findings are consistent with a number of previous studies on small-scale convection (e.g. van Hunen et al., 2003; Davies et al., 2016). Our results also highlight the sensitivity of EDC to the geometry and material properties of the step, particularly continental thickness. When modelled as a viscous, rigid block, the continent provides a natural guide to downwelling flow and shapes the associated edge-driven cell. The remaining geometrical parameters investigated (i.e. step width, age of oceanic plate and location of material boundary within

the step) influence the volume of lithospheric instabilities and the rate at which they develop, but their impact is secondary to that of continental thickness.

The 3-D distribution of lithospheric steps and their relative orientation exert a key control on the system's dynamics: edge-driven cells at steps that are in close proximity can coalesce and, thereby, enhance and localise upwelling flow, with our models yielding upwelling velocities up to 70 % higher than would otherwise be the case. In addition, cells are strongly sensitive to the magnitude and orientation of background mantle flow. Upwelling currents are strengthened through SDU where asthenospheric mantle flows away from the continent, but are suppressed where the asthenosphere flows toward the continent. Such results demonstrate that whilst lithospheric steps are an essential prerequisite for the development of edge-driven cells, the orientation and strength of background mantle flow determines whether or not these cells can form. This behaviour has a direct consequence on where melting can occur and how much melt can be produced. As an example, even though the structure of the indent is the same in all 3-D cases for which we prescribe background flow, the orientation of the velocity field, relative to the continent, leads to a factor of four variation in the cumulative melt production at the indent's lower-left corner (Table 3), thereby promoting or impeding surface volcanism.

The strong sensitivity of edge-driven convection and the associated melting to asthenospheric flow has important implications for our understanding of spatial and temporal patterns of intra-plate volcanism at lithospheric steps. In Earth's vigorously convecting mantle, asthenospheric flow directions and magnitudes are likely to be time-dependent (e.g. Coltice et al., 2018; Iaffaldano et al., 2018; Coltice et al., 2019), with a strong sensitivity to changes in plate motion (e.g. Müller et al., 2016) and the shallow Poiseuille component of mantle flow (e.g. Phipps Morgan et al., 1995; Höink et al., 2011; Stotz et al., 2017, 2018). Our simulations suggest that these changes in asthenospheric flow directions and magnitudes will strongly modulate edge-driven cells and the associated magmatism. To illustrate this, we present results from an additional 3-D simulation in Figure S9, where the plate motion direction has been rotated by 90° after 15 Myr. In such a scenario, edge-driven flow and the associated magmatism could be enhanced, reduced or even suppressed, within only a few million years of the plate motion change, at any given location along a lithospheric step. In particular, within 12 Myr, an edge that was originally orientated parallel to background mantle flow records a clear and substantial increase (decrease) in melt production as it has transitioned to a trailing (leading) edge. We note that these trends are visible in our melting diagnostics within only a few million years of the plate motion change. It is noteworthy that the original leading edge does not display a substantial increase in melt production following the plate motion change, suggesting a longer lag for steps dominated by downwelling currents prior to a change in the background flow direction. This is supported by the fact that the original trailing edge displays slightly enhanced melting than would be expected for a lateral edge, pointing towards a history dependence in the system. It is apparent, therefore, that under such a scenario, the history of mantle flow and the associated melting becomes important to understand why specific locations generate melt production trends that deviate from their expected behaviour. This additional observation reinforces the view on why volcanic provinces likely controlled by edge-driven convection are often short lived and time-dependent. We note that these mechanisms are in addition to those identified in previous studies that lead to a periodicity in edge-driven melting (e.g. Kaislaniemi & van Hunen, 2014).

In general, our results support EDC and SDU as a viable mechanism for intra-plate volcanism, particularly where the geometry, material properties and orientation of lithospheric steps, relative to each other and asthenospheric mantle flow, are favourable. Over a period of 15 Myr, our models neglecting the role of background mantle flow predict melt thicknesses of up to 0.24 km adjacent to continental margins, up to 0.59 km at an indent's internal corner, and 0.88 km inside the anomalous continental trough of our more com-

plex LAB case (Table 3). When background flow is incorporated, trailing edges, where underlying mantle flows away from the continent, record up to 0.33 km, while production at the indent's internal corners increases up to 0.7 km. Further horizontal integration of the cumulative melt thicknesses adjacent to such a corner yields reasonably consistent melt volumes for all cases that neglect background flow. These predicted volumes, however, are strongly modulated by the orientation of background flow: the largest volume predicted over 15 Myr of model evolution is 5403 km^3 within an area of 17,722 km^2 (Table 3), for the 3-D oblique case. Such a volume corresponds to a mean magmatic production rate of $\sim$0.36 $km^3\,kyr^{-1}$. However, as noted for the 2-D cases in Figures 6 and S4, the presence of background flow retards the development of secondary instabilities, and, hence, increased melt generation rates are only sustained for the first $\sim$20 Myr of model evolution, after which they drop as the lithospheric lid thickens. Taken together, these results demonstrate the central role played by both continental geometry and asthenospheric flow in dictating the characteristics of edge-driven flow and associated magmatism.

Our predicted melting volumes and rates suggest that EDC and SDU are suitable mechanisms only for Earth's lower-volume intra-plate volcanic provinces: they are unable to explain, for example, eruptive rates at the Hawaiian Ridge, Iceland or Cape Verde, which exceed 10 $km^3\,kyr^{-1}$ (e.g. Thordarson & Larsen, 2007; Holm et al., 2008; Wessel, 2016). However, a magmatic rate of $\sim$0.36 $km^3\,kyr^{-1}$ is comparable to rates determined for a number of smaller intra-plate volcanic provinces, including the Newer Volcanics Province of Victoria and South Australia, the old Springerville volcanic field within the southern Colorado Plateau, and the Siroua volcanic field of the Morrocan Atlas Mountains, all of which exhibit a long-term eruptive flux of $< 0.2\,km^3\,kyr^{-1}$ (van den Hove et al., 2017; Cas et al., 2017; Condit et al., 1989; Missenard & Cadoux, 2012).

It is important to emphasise, however, that such comparisons should be nuanced: all numerical models have limitations and many of our chosen parameters may not be appropriate at these locations. For example: (i) In our melting calculations, for simplicity, we assume a peridotitic composition – magmatism may be locally enhanced (or reduced) through the presence of more enriched (or depleted) compositions. Furthermore, we assume a wet peridotite batch melting parameterization and make no attempt to simulate the dynamics of melt transport and extraction; (ii) In our 3-D simulations, we set the initial depth of oceanic lithosphere to $\sim$90 km, which increases over time through thermal diffusion, while many of the aforementioned provinces are located above thinner lithosphere, which would increase predicted melting rates and volumes (e.g. Davies & Rawlinson, 2014; Priestley et al., 2018); (iii) We model the continent as a rigid and viscous block, that is not dramatically impacted by edge-driven processes – it is possible that parts of the continental edge behave weakly, modifying the edge-driven process and associated melting (e.g. Liu & Chen, 2019); (iv) Our study has focused on simulations with short evolution times, to isolate the sensitivity of EDC and SDU to the controlling parameters examined. In reality, lithospheric steps, particularly those at cratonic margins, are likely long-lived (e.g. Hoggard et al., 2020). Simulations with longer evolution times develop secondary instabilities that make it more difficult to isolate the signals highlighted herein. Nonetheless, as illustrated in Figure S5, which compares both flow dynamics and melting patterns for Case U400 after 15 Myr and 30 Myr, the first order trends highlighted herein would likely remain consistent; (v) The strength and scale of edge-driven cells in our simulations is strongly dependent on the magnitude and depth-dependence of viscosity, which remain uncertain (Korenaga & Karato, 2008; Paulson & Richards, 2009; Iaffaldano & Lambeck, 2014; Rudolph et al., 2015). Nonetheless, we examined the sensitivity of our results under a range of different scenarios, all of which are within the estimated range (Lau et al., 2016); and (vi) We neglect other important aspects of mantle convection, including compressibility (Gassmöller et al., 2020), phase transitions (Tackley et al., 1993), global mantle flow and mantle plumes.

Each of the previous points requires further investigation to quantify their effect on the flow field and associated melting rates and melt volumes. Nonetheless, our results suggest that EDC and SDU are capable of generating volcanic rates on the order of $\sim 1\,\mathrm{km^3\,kyr^{-1}}$ under favourable conditions. As highlighted above, this is consistent with the rates determined for a number of intra-plate volcanic provinces on Earth that lie adjacent to step-changes in lithospheric thickness, supporting EDC and SDU as a viable mechanism. At other provinces, which exhibit substantially enhanced melting rates, alternative mechanisms, such as mantle plumes, are likely more applicable. Indeed, there is increasing evidence that the shallow mechanisms examined herein interact with upwelling mantle plumes in some locations, to produce complex volcanic patterns at the surface (e.g. Davies et al., 2015; Rawlinson et al., 2017; Kennett & Davies, 2020). Understanding these interactions is an important avenue for future research.

5 Conclusion

This study systematically documents the behaviour of EDC and SDU in 2-D and 3-D geodynamical models. Our 2-D simulations demonstrate that EDC results from the negative buoyancy of lithospheric mantle adjacent to a rigid continental block at a lithospheric step. EDC is sensitive to the geometry and material properties of that step, in addition to the upper mantle viscosity profile: given sufficient space, EDC cells can develop at viscosities below $10^{20}\,\mathrm{Pa\,s}$. However, if viscosities are higher, or the low-viscosity asthenosphere is restricted to a narrow channel, an EDC cell does not develop.

By examining a set of different continental geometries in our 3-D models, we have demonstrated that edge-driven cells, adjacent to lithospheric steps that are in close proximity, can influence each other and, thereby, lead to enhanced, localised upwelling. Additionally, by prescribing a range of background mantle flow orientations, we have shown that these upwellings can either be enhanced by SDU, where the asthenosphere flows away from the continent, or suppressed by sub-lithospheric currents heading toward the continent. In our models, these flow patterns are mirrored in melting trends, as melting occurs purely through decompression. The predicted melt volumes suggest that, in the absence of potential interactions with mantle plumes, EDC and SDU are viable mechanisms only for Earth's shorter-lived and lower-volume intra-plate volcanic provinces. Taken together, our results illustrate the importance of local variations in lithospheric thickness and the orientation and magnitude of asthenospheric flow in controlling the location and timing of EDC and SDU-generated intra-plate volcanism. A key outcome of this study is that, although changes in lithospheric thickness provide a favourable setting for EDC, these cells can be displaced and overwhelmed by background mantle flow. As such, our study helps to explain why step changes in lithospheric thickness, which are common along cratonic edges and passive margins, only produce volcanism at isolated points in space and time.

Acknowledgments

T.D. is funded by an ANU PhD Scholarship (International) Full-Time (737/2018). D.R.D. acknowledges support from the Australian Research Council (ARC), under FT140101262. C.R.M is funded by an Australian Government Research Training Program Domestic Scholarship. D.R.D., S.C.K. and T.D. acknowledge support from the ARC under DP170100058. Numerical simulations were undertaken on the NCI National Facility in Canberra, Australia, which is supported by the Australian Commonwealth Government. The Fluidity computational modelling framework, including source code and documentation, is available from `https://fluidityproject.github.io/`; the latest release, with tag 4.1.17 and which we used for the simulations presented herein, is archived at `https://doi.org/10.5281/zenodo.3988620`. The authors would like to thank Patrick Ball, Brian Kennett, Ian Campbell, Marthe Klöcking and Siavash Ghelichkan for fruitful discussions at various stages of this research.

References

Afonso, J. C., Rawlinson, N., Yang, Y., Schutt, D. L., Jones, A. G., Fullea, J., & Griffin, W. L. (2016). 3-D multiobservable probabilistic inversion for the compositional and thermal structure of the lithosphere and upper mantle: III. Thermochemical tomography in the Western-Central US. *Journal of Geophysical Research: Solid Earth*, *121*(10), 7337–7370.

Artemieva, I. M. (2009). The continental lithosphere: reconciling thermal, seismic, and petrologic data. *Lithos*, *109*(1-2), 23–46.

Ballmer, M. D., Conrad, C. P., Smith, E. I., & Harmon, N. (2013). Non-hotspot volcano chains produced by migration of shear-driven upwelling toward the East Pacific Rise. *Geology*, *41*(4), 479–482.

Ballmer, M. D., Conrad, C. P., Smith, E. I., & Johnsen, R. (2015). Intraplate volcanism at the edges of the Colorado Plateau sustained by a combination of triggered edge-driven convection and shear-driven upwelling. *Geochemistry, Geophysics, Geosystems*, *16*(2), 366–379.

Ballmer, M. D., Ito, G., Van Hunen, J., & Tackley, P. J. (2011). Spatial and temporal variability in Hawaiian hotspot volcanism induced by small-scale convection. *Nature Geoscience*, *4*(7), 457–460.

Bianco, T. A., Conrad, C. P., & Smith, E. I. (2011). Time dependence of intraplate volcanism caused by shear-driven upwelling of low-viscosity regions within the asthenosphere. *Journal of Geophysical Research: Solid Earth*, *116*(B11).

Boyce, J. (2013). The Newer Volcanics Province of southeastern Australia: a new classification scheme and distribution map for eruption centres. *Australian Journal of Earth Sciences*, *60*(4), 449–462.

Bredow, E., Steinberger, B., Gassmöller, R., & Dannberg, J. (2017). How plume-ridge interaction shapes the crustal thickness pattern of the Réunion hotspot track. *Geochemistry, Geophysics, Geosystems*, *18*(8), 2930–2948.

Brent, R. P. (2013). *Algorithms for minimization without derivatives*. Courier Corporation.

Buck, W. R. (1986). Small-scale convection induced by passive rifting: the cause for uplift of rift shoulders. *Earth and Planetary Science Letters*, *77*(3-4), 362–372.

Cas, R., Van Otterloo, J., Blaikie, T., & Van Den Hove, J. (2017). The dynamics of a very large intra-plate continental basaltic volcanic province, the Newer Volcanics Province, SE Australia, and implications for other provinces. *Geological Society, London, Special Publications*, *446*(1), 123–172.

Coltice, N., Husson, L., Faccenna, C., & Arnould, M. (2019). What drives tectonic plates? *Science advances*, *5*(10), eaax4295.

Coltice, N., Larrouturou, G., Debayle, E., & Garnero, E. J. (2018). Interactions of scales of convection in the Earth's mantle. *Tectonophysics*, *746*, 669–677.

Condit, C. D., Crumpler, L., Aubele, J. C., & Elston, W. E. (1989). Patterns of volcanism along the southern margin of the Colorado Plateau: The Springerville field. *Journal of Geophysical Research: Solid Earth*, *94*(B6), 7975–7986.

Conrad, C. P., Bianco, T. A., Smith, E. I., & Wessel, P. (2011). Patterns of intraplate volcanism controlled by asthenospheric shear. *Nature Geoscience*, *4*(5), 317–321.

Conrad, C. P., Wu, B., Smith, E. I., Bianco, T. A., & Tibbetts, A. (2010). Shear-driven upwelling induced by lateral viscosity variations and asthenospheric shear: A mechanism for intraplate volcanism. *Physics of the Earth and Planetary Interiors*, *178*(3-4), 162–175.

Courtillot, V., Davaille, A., Besse, J., & Stock, J. (2003). Three distinct types of hotspots in the Earth's mantle. *Earth and Planetary Science Letters*, *205*(3-4), 295–308.

Currie, C. A., & van Wijk, J. (2016). How craton margins are preserved: Insights from geodynamic models. *Journal of Geodynamics*, *100*, 144–158.

Davies, D. R., & Davies, J. H. (2009). Thermally-driven mantle plumes reconcile multiple hot-spot observations. *Earth and Planetary Science Letters*, *278*(1-2), 50–54.

Davies, D. R., Le Voci, G., Goes, S., Kramer, S. C., & Wilson, C. R. (2016). The mantle wedge's transient 3-D flow regime and thermal structure. *Geochemistry, Geophysics, Geosystems*, *17*(1), 78–100.

Davies, D. R., & Rawlinson, N. (2014). On the origin of recent intraplate volcanism in Australia. *Geology*, *42*(12), 1031–1034.

Davies, D. R., Rawlinson, N., Iaffaldano, G., & Campbell, I. H. (2015). Lithospheric controls on magma composition along Earth's longest continental hotspot track. *Nature*, *525*(7570), 511–514.

Davies, D. R., Wilson, C. R., & Kramer, S. C. (2011). Fluidity: A fully unstructured anisotropic adaptive mesh computational modeling framework for geodynamics. *Geochemistry, Geophysics, Geosystems*, *12*(6).

Demidjuk, Z., Turner, S., Sandiford, M., George, R., Foden, J., & Etheridge, M. (2007). U-series isotope and geodynamic constraints on mantle melting processes beneath the Newer Volcanic Province in South Australia. *Earth and Planetary Science Letters*, *261*(3), 517–533.

Farnetani, C. G., & Richards, M. A. (1995). Thermal entrainment and melting in mantle plumes. *Earth and Planetary Science Letters*, *136*(3-4), 251–267.

Farrington, R., Stegman, D., Moresi, L., Sandiford, M., & May, D. (2010). Interactions of 3D mantle flow and continental lithosphere near passive margins. *Tectonophysics*, *483*(1-2), 20–28.

Fjeldskaar, W., & Cathles, L. (1991). The present rate of uplift of Fennoscandia implies a low-viscosity asthenosphere. *Terra Nova*, *3*(4), 393–400.

French, S. W., & Romanowicz, B. (2015). Broad plumes rooted at the base of the Earth's mantle beneath major hotspots. *Nature*, *525*(7567), 95.

Garel, F., Goes, S., Davies, D. R., Davies, J. H., Kramer, S. C., & Wilson, C. R. (2014). Interaction of subducted slabs with the mantle transition-zone: A regime diagram from 2-D thermo-mechanical models with a mobile trench and an overriding plate. *Geochemistry, Geophysics, Geosystems*, *15*(5), 1739–1765.

Gassmöller, R., Dannberg, J., Bangerth, W., Heister, T., & Myhill, R. (2020). On formulations of compressible mantle convection. *Geophysical Journal International*, *221*(2), 1264–1280.

Gibert, B., Seipold, U., Tommasi, A., & Mainprice, D. (2003). Thermal diffusivity of upper mantle rocks: Influence of temperature, pressure, and the deformation fabric. *Journal of Geophysical Research: Solid Earth*, *108*(B8).

Hirth, G., & Kohlstedt, D. (2004). Rheology of the upper mantle and the mantle wedge: A view from the experimentalists. *Inside the Subduction Factory*, *138*, 83–105.

Hoggard, M. J., Czarnota, K., Richards, F. D., Huston, D. L., Jaques, A. L., & Ghelichkhan, S. (2020). Global distribution of sediment-hosted metals controlled by craton edge stability. *Nature Geoscience*, *13*(7), 504–510.

Höink, T., Jellinek, A. M., & Lenardic, A. (2011). Viscous coupling at the lithosphere-asthenosphere boundary. *Geochemistry, Geophysics, Geosystems*, *12*(10).

Höink, T., & Lenardic, A. (2010). Long wavelength convection, Poiseuille–Couette flow in the low-viscosity asthenosphere and the strength of plate margins. *Geophysical Journal International*, *180*(1), 23–33.

Holm, P. M., Grandvuinet, T., Friis, J., Wilson, J. R., Barker, A. K., & Plesner, S. (2008). An 40Ar-39Ar study of the Cape Verde hot spot: Temporal evolution in a semistationary plate environment. *Journal of Geophysical Research: Solid Earth*, *113*(B8).

Iaffaldano, G., Davies, D., & DeMets, C. (2018). Indian ocean floor deformation induced by the Reunion plume rather than the Tibetan Plateau. *Nature Geo-*

science, *11*(5), 362–366.

Iaffaldano, G., & Lambeck, K. (2014). Pacific plate-motion change at the time of the Hawaiian-Emperor bend constrains the viscosity of Earth's asthenosphere. *Geophysical Research Letters*, *41*(10), 3398–3406.

Jaupart, C., & Mareschal, J. (2005). Production from heat flow data. *The Crust*, *3*, 65–84.

Jaupart, C., Mareschal, J.-C., Guillou-Frottier, L., & Davaille, A. (1998). Heat flow and thickness of the lithosphere in the Canadian Shield. *Journal of Geophysical Research: Solid Earth*, *103*(B7), 15269–15286.

Jones, T., Davies, D. R., Campbell, I., Iaffaldano, G., Yaxley, G., Kramer, S., & Wilson, C. (2017). The concurrent emergence and causes of double volcanic hotspot tracks on the Pacific plate. *Nature*, *545*(7655), 472.

Kaban, M. K., Schwintzer, P., Artemieva, I. M., & Mooney, W. D. (2003). Density of the continental roots: compositional and thermal contributions. *Earth and Planetary Science Letters*, *209*(1-2), 53–69.

Kaislaniemi, L., & van Hunen, J. (2014). Dynamics of lithospheric thinning and mantle melting by edge-driven convection: Application to Moroccan Atlas mountains. *Geochemistry, Geophysics, Geosystems*, *15*(8), 3175–3189.

Katsura, T., Yoneda, A., Yamazaki, D., Yoshino, T., & Ito, E. (2010). Adiabatic temperature profile in the mantle. *Physics of the Earth and Planetary Interiors*, *183*(1-2), 212–218.

Katz, R. F., Spiegelman, M., & Langmuir, C. H. (2003). A new parameterization of hydrous mantle melting. *Geochemistry, Geophysics, Geosystems*, *4*(9).

Kennett, B., & Davies, D. (2020). Intra-plate volcanism in North Queensland and eastern new Guinea: A cryptic mantle plume? *Gondwana Research*, *79*, 209–216.

King, S. D., & Anderson, D. L. (1998). Edge-driven convection. *Earth and Planetary Science Letters*, *160*(3-4), 289–296.

Korenaga, J., & Karato, S.-I. (2008). A new analysis of experimental data on olivine rheology. *Journal of Geophysical Research: Solid Earth*, *113*(B2).

Kramer, S. C., Wilson, C. R., & Davies, D. R. (2012). An implicit free surface algorithm for geodynamical simulations. *Physics of the Earth and Planetary Interiors*, *194*, 25–37.

Lachenbruch, A. H. (1970). Crustal temperature and heat production: Implications of the linear heat-flow relation. *Journal of Geophysical Research*, *75*(17), 3291–3300.

Lau, H. C., Mitrovica, J. X., Austermann, J., Crawford, O., Al-Attar, D., & Latychev, K. (2016). Inferences of mantle viscosity based on ice age data sets: Radial structure. *Journal of Geophysical Research: Solid Earth*, *121*(10), 6991–7012.

Lenardic, A., & Moresi, L.-N. (1999). Some thoughts on the stability of cratonic lithosphere: Effects of buoyancy and viscosity. *Journal of Geophysical Research: Solid Earth*, *104*(B6), 12747–12758.

Lenardic, A., Moresi, L.-N., & Mühlhaus, H. (2003). Longevity and stability of cratonic lithosphere: insights from numerical simulations of coupled mantle convection and continental tectonics. *Journal of Geophysical Research: Solid Earth*, *108*(B6).

Le Voci, G., Davies, D. R., Goes, S., Kramer, S. C., & Wilson, C. R. (2014). A systematic 2-D investigation into the mantle wedge's transient flow regime and thermal structure: Complexities arising from a hydrated rheology and thermal buoyancy. *Geochemistry, Geophysics, Geosystems*, *15*(1), 28–51.

Liu, D., & Chen, L. (2019). Edge-driven convection and thinning of craton lithosphere: Two-dimensional thermal-mechanical modeling. *Science China Earth Sciences*, *62*(12), 2106–2120.

McKenzie, D., Jackson, J., & Priestley, K. (2005). Thermal structure of oceanic and

902 continental lithosphere. *Earth and Planetary Science Letters*, *233*(3-4), 337–
903 349.
904 McLaren, S., Sandiford, M., Hand, M., Neumann, N., Wyborn, L., & Bastrakova,
905 I. (2003). The hot southern continent: heat flow and heat production in Aus-
906 tralian Proterozoic terranes. *Special Papers-geological Society of America*,
907 157–168.
908 Métivier, L., Caron, L., Greff-Lefftz, M., Pajot-Métivier, G., Fleitout, L., & Rouby,
909 H. (2016). Evidence for postglacial signatures in gravity gradients: A clue in
910 lower mantle viscosity. *Earth and Planetary Science Letters*, *452*, 146–156.
911 Missenard, Y., & Cadoux, A. (2012). Can Moroccan Atlas lithospheric thinning and
912 volcanism be induced by edge-driven convection? *Terra Nova*, *24*(1), 27–33.
913 Mitrovica, J. X., & Forte, A. (2004). A new inference of mantle viscosity based upon
914 joint inversion of convection and glacial isostatic adjustment data. *Earth and*
915 *Planetary Science Letters*, *225*(1-2), 177–189.
916 Morgan, W. J. (1971). Convection plumes in the lower mantle. *Nature*, *230*(5288),
917 42.
918 Morgan, W. J. (1972). Deep mantle convection plumes and plate motions. *AAPG*
919 *bulletin*, *56*(2), 203–213.
920 Müller, R. D., Seton, M., Zahirovic, S., Williams, S. E., Matthews, K. J., Wright,
921 N. M., ... others (2016). Ocean basin evolution and global-scale plate reorga-
922 nization events since Pangea breakup. *Annual Review of Earth and Planetary*
923 *Sciences*, *44*, 107–138.
924 Naif, S., Key, K., Constable, S., & Evans, R. (2013). Melt-rich channel observed at
925 the lithosphere–asthenosphere boundary. *Nature*, *495*(7441), 356.
926 Neumann, N., Sandiford, M., & Foden, J. (2000). Regional geochemistry and conti-
927 nental heat flow: implications for the origin of the South Australian heat flow
928 anomaly. *Earth and Planetary Science Letters*, *183*(1-2), 107–120.
929 Nicolaysen, L., Hart, R., & Gale, N. (1981). The Vredefort radioelement profile
930 extended to supracrustal strata at Carletonville, with implications for con-
931 tinental heat flow. *Journal of Geophysical Research: Solid Earth*, *86*(B11),
932 10653–10661.
933 Parsons, B., & Sclater, J. G. (1977). An analysis of the variation of ocean floor
934 bathymetry and heat flow with age. *Journal of geophysical research*, *82*(5),
935 803–827.
936 Paulson, A., & Richards, M. A. (2009). On the resolution of radial viscosity struc-
937 ture in modelling long-wavelength postglacial rebound data. *Geophysical Jour-*
938 *nal International*, *179*(3), 1516–1526.
939 Peacock, S. A. (1990). Fluid processes in subduction zones. *Science*, *248*(4953),
940 329–337.
941 Phipps Morgan, J., Morgan, W. J., Zhang, Y.-S., & Smith, W. H. (1995). Ob-
942 servational hints for a plume-fed, suboceanic asthenosphere and its role in
943 mantle convection. *Journal of Geophysical Research: Solid Earth*, *100*(B7),
944 12753–12767.
945 Phipps Morgan, J., Parmentier, E., & Lin, J. (1987). Mechanisms for the origin of
946 mid-ocean ridge axial topography: Implications for the thermal and mechani-
947 cal structure of accreting plate boundaries. *Journal of Geophysical Research:*
948 *Solid Earth*, *92*(B12), 12823–12836.
949 Pollack, H. N., & Chapman, D. S. (1977). On the regional variation of heat flow,
950 geotherms, and lithospheric thickness. *Tectonophysics*, *38*(3-4), 279–296.
951 Priestley, K., McKenzie, D., & Ho, T. (2018). A lithosphere–asthenosphere
952 boundary–a global model derived from multimode surface-wave tomography
953 and petrology. *Lithospheric discontinuities*, 111–123.
954 Putirka, K. (2016). Rates and styles of planetary cooling on Earth, Moon, Mars, and
955 Vesta, using new models for oxygen fugacity, ferric-ferrous ratios, olivine-liquid
956 Fe-Mg exchange, and mantle potential temperature. *American Mineralogist*,

101(4), 819–840.

Rawlinson, N., Davies, D. R., & Pilia, S. (2017). The mechanisms underpinning Cenozoic intraplate volcanism in eastern Australia: Insights from seismic tomography and geodynamic modeling. *Geophysical Research Letters*, *44*(19), 9681–9690.

Richards, M. A., Duncan, R. A., & Courtillot, V. E. (1989). Flood basalts and hotspot tracks: plume heads and tails. *Science*, *246*(4926), 103–107.

Richards, M. A., & Griffiths, R. W. (1989). Thermal entrainment by deflected mantle plumes. *Nature*, *342*(6252), 900.

Richards, M. A., Yang, W.-S., Baumgardner, J. R., & Bunge, H.-P. (2001). Role of a low-viscosity zone in stabilizing plate tectonics: Implications for comparative terrestrial planetology. *Geochemistry, Geophysics, Geosystems*, *2*(8).

Rolf, T., Capitanio, F. A., & Tackley, P. J. (2018). Constraints on mantle viscosity structure from continental drift histories in spherical mantle convection models. *Tectonophysics*, *746*, 339–351.

Rudolph, M. L., Lekić, V., & Lithgow-Bertelloni, C. (2015). Viscosity jump in Earth's mid-mantle. *Science*, *350*(6266), 1349–1352.

Sarafian, E., Gaetani, G. A., Hauri, E. H., & Sarafian, A. R. (2017). Experimental constraints on the damp peridotite solidus and oceanic mantle potential temperature. *Science*, *355*(6328), 942–945.

Schatz, J. F., & Simmons, G. (1972). Thermal conductivity of earth materials at high temperatures. *Journal of Geophysical Research*, *77*(35), 6966–6983.

Sengör, A., & Burke, K. (1978). Relative timing of rifting and volcanism on Earth and its tectonic implications. *Geophysical Research Letters*, *5*(6), 419–421.

Stotz, I. L., Iaffaldano, G., & Davies, D. R. (2017). Late Miocene Pacific plate kinematic change explained with coupled global models of mantle and lithosphere dynamics. *Geophysical Research Letters*, *44*, 7177-7186.

Stotz, I. L., Iaffaldano, G., & Davies, D. R. (2018). Pressure-driven Poiseuille flow: A major component of the torque-balance governing Pacific plate motion. *Geophysical Research Letters*, *45*(1), 117–125.

Tackley, P. J., Stevenson, D. J., Glatzmaier, G. A., & Schubert, G. (1993). Effects of an endothermic phase transition at 670 km depth in a spherical model of convection in the earth's mantle. *Nature*, *361*(6414), 699.

Tatsumi, Y., Hamilton, D., & Nesbitt, R. (1986). Chemical characteristics of fluid phase released from a subducted lithosphere and origin of arc magmas: evidence from high-pressure experiments and natural rocks. *Journal of Volcanology and Geothermal Research*, *29*(1-4), 293–309.

Thompson, G. A., & Zoback, M. L. (1979). Regional geophysics of the Colorado Plateau. *Tectonophysics*, *61*(1-3), 149–181.

Thordarson, T., & Larsen, G. (2007). Volcanism in Iceland in historical time: Volcano types, eruption styles and eruptive history. *Journal of Geodynamics*, *43*(1), 118–152.

Till, C. B., Elkins-Tanton, L. T., & Fischer, K. M. (2010). A mechanism for low-extent melts at the lithosphere-asthenosphere boundary. *Geochemistry, Geophysics, Geosystems*, *11*(10).

Turcotte, D., & Oxburgh, E. R. (1978). Intra-plate volcanism. *Philosophical Transactions of the Royal Society of London. Series A, Mathematical and Physical Sciences*, *288*(1355), 561–579.

van den Hove, J. C., Van Otterloo, J., Betts, P. G., Ailleres, L., & Cas, R. A. (2017). Controls on volcanism at intraplate basaltic volcanic fields. *Earth and Planetary Science Letters*, *459*, 36–47.

van Hunen, J., Huang, J., & Zhong, S. (2003). The effect of shearing on the onset and vigor of small-scale convection in a Newtonian rheology. *Geophysical research letters*, *30*(19).

Wang, H., van Hunen, J., Pearson, D. G., & Allen, M. B. (2014). Craton stability

and longevity: The roles of composition-dependent rheology and buoyancy. *Earth and Planetary Science Letters*, *391*, 224–233.

Wessel, P. (2016). Regional–residual separation of bathymetry and revised estimates of Hawaii plume flux. *Geophysical Journal International*, *204*(2), 932–947.

Whittington, A. G., Hofmeister, A. M., & Nabelek, P. I. (2009). Temperature-dependent thermal diffusivity of the Earth's crust and implications for magmatism. *Nature*, *458*(7236), 319.

Wilson, C. (2009). *Modelling multiple-material flows on adaptive unstructured meshes* (Unpublished doctoral dissertation). Imperial College London.

Ye, Y., Schwering, R. A., & Smyth, J. R. (2009). Effects of hydration on thermal expansion of forsterite, wadsleyite, and ringwoodite at ambient pressure. *American Mineralogist*, *94*(7), 899–904.